

Astrophysical interpretation of the anisotropies in the unresolved gamma-ray background

Shin'ichiro Ando,^{1,*} Mattia Fornasa,^{1,†} Nicolao Fornengo,^{2,3} Marco Regis,^{2,3} and Hannes-S. Zechlin^{2,3}

¹*GRAPPA, University of Amsterdam, Science Park, 1098 XH Amsterdam, The Netherlands*

²*Dipartimento di Fisica, Università di Torino, via P. Giuria 1, I-10125 Torino, Italy*

³*Istituto Nazionale di Fisica Nucleare, Sezione di Torino, via P. Giuria 1, I-10125 Torino, Italy*

(Dated: March 18, 2018)

Recently, a new measurement of the auto- and cross-correlation angular power spectrum (APS) of the isotropic gamma-ray background was performed, based on 81 months of data of the *Fermi* Large-Area Telescope (LAT). Here, we fit, for the first time, the new APS data with a model describing the emission of unresolved blazars. These sources are expected to dominate the anisotropy signal. The model we employ in our analysis reproduces well the blazars resolved by *Fermi* LAT. When considering the APS obtained by masking the sources in the 3FGL catalogue, we find that unresolved blazars under-produce the measured APS below ~ 1 GeV. Contrary to past results, this suggests the presence of a new contribution to the low-energy APS, with a significance of, at least, 5σ . The excess can be ascribed to a new class of faint gamma-ray emitters. If we consider the APS obtained by masking the sources in the 2FGL catalogue, there is no under-production of the APS below 1 GeV, but the new source class is still preferred over the blazars-only scenario (with a significance larger than 10σ). The properties of the new source class and the level of anisotropies induced in the isotropic gamma-ray background are the same, independent of the APS data used. In particular, the new gamma-ray emitters must have a soft energy spectrum, with a spectral index ranging, approximately, from 2.7 to 3.2. This complicates their interpretation in terms of known sources, since, normally, star-forming and radio galaxies are observed with a harder spectrum. The new source class identified here is also expected to contribute significantly to the intensity of the isotropic gamma-ray background.

I. INTRODUCTION

In more than 8 years of operation, the *Fermi* Large Area Telescope (LAT) has significantly increased the census of known gamma-ray emitters: the most recent source catalogue (i.e., the *Fermi* LAT Third Source Catalogue, 3FGL) contains 3033 objects, detected with a significance greater than 4σ between 100 MeV and 300 GeV [1]. Gamma-ray sources that are too faint to be resolved individually by *Fermi* LAT contribute cumulatively to the so-called isotropic gamma-ray background (IGRB). See Ref. [2] for a recent review.

The most recent measurement of the intensity energy spectrum of the IGRB was performed by *Fermi* LAT and it covers the energy range between 0.1 and 820 GeV [3]. By modeling known classes of gamma-ray emitters, Ref. [4] showed that the measured energy spectrum of the IGRB can be explained by the concomitant emission of unresolved blazars, star-forming and radio galaxies. However, the exact composition of the IGRB is still unknown: reconstructing it would provide valuable insight on the characteristics of the contributing source classes.

Different populations of gamma-ray emitters are expected to induce different levels of anisotropies in the IGRB (see Refs. [5–12] among others). Thus, a measurement of the gamma-ray angular power spectrum

(APS) can constrain the nature of the IGRB in a complementary way with respect to the intensity energy spectrum. Other observables that can be employed to a similar goal are the 1-point photon count probability distribution of the IGRB [13–17], the cross correlation of the IGRB with catalogues of resolved galaxies [18–25] or of galaxy clusters [26], the cross-correlation with the weak gravitational lensing of cosmic shear [27–31] or with the gravitational lensing of the cosmic microwave background [32].

The first detection of the IGRB anisotropy APS was reported by the *Fermi* LAT Collaboration in 2012, in the energy range between 1 and 50 GeV [33]. The signal was compatible with being due *entirely* to unresolved blazars [9, 10, 12].

An updated measurement of the anisotropy APS has been recently released, employing 81 months of *Fermi* LAT data, binned in 13 energy bins, from 0.5 to 500 GeV [34]. Apart from the auto-correlation APS in each energy bin, the new analysis measured, for the first time, the cross-correlation APS between different energy bins. Ref. [34] suggested that the new APS data are due to more than one population of sources.

In this paper, we interpret the auto- and cross-correlation APS measured in Ref. [34] in terms of unresolved blazars. We employ a parametric model that was designed to describe the blazars observed by *Fermi* LAT [4, 35–37]. The result of our fit to the new APS measurement will determine whether the latter can still be explained in terms of blazars alone or if an additional population of gamma-ray emitters is needed.

* s.ando@uva.nl

† fornasa@gmail.com

Our analysis will also quantify the impact of the new APS measurement in constraining the properties of the blazar population, e.g., its redshift evolution and distribution in luminosity (especially at low luminosities). In general, this is the first work that takes advantage of the new anisotropy measurement to constrain the nature of the IGRB, employing physically-motivated models of astrophysical emitters.

The paper is organized as follows: in Sec. II, we summarize the model used to describe the blazar population. We also discuss how to compute the observables in which we are interested, i.e. the anisotropy APS of unresolved blazars, the source count distribution function of resolved blazars and the intensity energy spectrum of all blazars (both resolved and unresolved). In Sec. III, we present the data employed in the fit and we describe our fitting technique. The results are presented in Sec. IV, while Sec. V and Sec. VI are left for the discussion and the conclusions, respectively.

II. MODELING THE BLAZAR POPULATION

Refs. [4, 36, 37] model the blazar population by means of a parametric description of their gamma-ray luminosity function, of their redshift evolution and of their energy spectrum. Alternatively, in the “blazar-sequence” model, the whole spectral energy distribution of blazars is parametrized and their gamma-ray luminosity is related to the luminosity in X-rays [38, 39]. Here, we follow the former approach because we are interested in comparing our results directly to those of Ref. [4], in which the model parameters are constrained only by the properties of resolved blazars. Also, *Fermi* LAT has detected a significant number of sources to allow population studies to be performed entirely in gamma rays, without relying on a phenomenological correlation with X-rays.

The gamma-ray luminosity function of blazars, $\Phi(L_\gamma, z, \Gamma)$, is defined as the number of sources per unit of luminosity L_γ (defined in the rest frame of the source, for energies between 0.1 and 100 GeV), of comoving volume dV^1 and of spectral photon index Γ . The luminosity function at redshift $z = 0$ is modeled as a double power law in L_γ , as follows:

$$\begin{aligned} \Phi(L_\gamma, z = 0, \Gamma) &= \frac{dN}{dL_\gamma dV d\Gamma} \\ &= \frac{A}{\ln(10)L_\gamma} \left[\left(\frac{L_\gamma}{L_0} \right)^{\gamma_1} + \left(\frac{L_\gamma}{L_0} \right)^{\gamma_2} \right]^{-1} \\ &\quad \times \exp \left[-\frac{(\Gamma - \mu(L_\gamma))^2}{2\sigma^2} \right], \end{aligned} \quad (1)$$

where γ_1 and γ_2 are the indexes of the power laws and L_0 controls the transition between the two regimes. The factor A sets the overall normalization and the exponential term describes a Gaussian distribution for the photon index Γ , with $\mu(L_\gamma)$ and σ its mean and rms, respectively.

In the literature, blazars are often divided into two subclasses, flat-spectrum radio quasars (FSRQs) and BL Lacertae objects (BL Lacs). The two subclasses populate different regimes of the same correlation between luminosity and spectral index: FSRQs are brighter with a softer spectrum but, as the luminosity decreases, sources become harder and it is more common to find BL Lacs than FSRQs [41]. Allowing for the mean $\mu(L_\gamma)$ of the spectral-index distribution to depend on L_γ , one can reproduce the L_γ - Γ correlation and, thus, describe both FSRQs and BL Lacs with the same model. In particular, we assume $\mu(L_\gamma)$ to be parametrized as follows [4, 42, 43]:

$$\mu(L_\gamma) = \mu^* + \beta \left[\log \left(\frac{L_\gamma}{\text{erg s}^{-1}} \right) - 46 \right]. \quad (2)$$

The redshift evolution of the gamma-ray luminosity function is described by the evolutionary factor $e(L_\gamma, z)$ [4, 36],

$$\Phi(L_\gamma, z, \Gamma) = \Phi(L_\gamma, z = 0, \Gamma) e(z, L_\gamma), \quad (3)$$

with

$$\begin{aligned} e(z, L_\gamma) &= \left[\left(\frac{1+z}{1+z_c(L_\gamma)} \right)^{-p_1(L_\gamma)} \right. \\ &\quad \left. + \left(\frac{1+z}{1+z_c(L_\gamma)} \right)^{-p_2(L_\gamma)} \right]^{-1}. \end{aligned} \quad (4)$$

The parameters in Eq. (4) depend on the luminosity as follows:

$$z_c(L_\gamma) = z_c^* \left(\frac{L_\gamma}{10^{48} \text{ erg s}^{-1}} \right)^\alpha, \quad (5)$$

$$p_1(L_\gamma) = p_1^0 + \tau \left[\log \left(\frac{L_\gamma}{\text{erg s}^{-1}} \right) - 44 \right], \quad (6)$$

$$p_2(L_\gamma) = p_2^0 + \delta \left[\log \left(\frac{L_\gamma}{\text{erg s}^{-1}} \right) - 44 \right]. \quad (7)$$

The indexes $p_1(L_\gamma)$ and $p_2(L_\gamma)$ control the redshift evolution of blazars, with a positive (negative) index corresponding to a positive (negative) evolution, i.e., the gamma-ray luminosity function increasing (decreasing) with z . The critical redshift z_c determines the epoch of transition between the two evolutionary regimes.

Eqs. (3)–(7) describe the so-called luminosity-dependent density evolution (LDDE). Other evolutionary scenarios, with different $e(z, L_\gamma)$ and modified versions of Eq. (3) have been considered in the literature. Ref. [4] employs them to describe a sample of 403 blazars detected by *Fermi* LAT with a test statistics larger than

¹ We employ cosmological parameters in agreement with the observations by Planck [40].

50, at Galactic latitudes $|b|$ larger than 15° [44]. Even if the analysis of Ref. [4] is not able to significantly prefer one evolutionary scheme over the other, the LDDE is the one yielding the best description of the sample of blazars. Thus, in this work, we restrict our analysis to the LDDE scheme.

Blazars are best described by a curved energy spectrum. Thus, we model their energy spectrum dN_γ/dE as follows:

$$\frac{dN_\gamma}{dE_\gamma} \propto \left[\left(\frac{E_\gamma}{E_b} \right)^{\gamma_a} + \left(\frac{E_\gamma}{E_b} \right)^{\gamma_b} \right]^{-1} \exp[-\tau(E_\gamma, z)] \quad (8)$$

and we assume that E_b correlates with Γ according to $\log(E_b/\text{GeV}) = 9.25 - 4.11\Gamma$ [4]. The factor $\exp[-\tau(E_\gamma, z)]$ accounts for the absorption of gamma rays due to pair conversion with the extragalactic background light. We model it following Ref. [45].

According to the model defined above, the differential source count distribution of blazars dN/dF (i.e. the number of sources per unit solid angle and per unit flux, measured in $\text{cm}^2 \text{s deg}^{-2}$) can be written as follows:

$$\frac{dN}{dF} = \int_{0.01}^{5.0} dz \int_1^{3.5} d\Gamma \Phi[L_\gamma(F_E, z, \Gamma), z, \Gamma] \frac{dV}{dz} \frac{dL_\gamma}{dF}, \quad (9)$$

where F denotes the flux above 100 MeV and F_E indicates the *energy* flux, as opposed to the *number* flux F . The quantity $L_\gamma(F_E, z, \Gamma)$ is the luminosity associated with a source with flux F_E at a redshift z and with spectral index Γ . The bounds of the integration in Γ in Eq. (9) are chosen to properly sample the distribution of Γ , while those in redshift probe the region where the majority of the emission comes from. In particular, we assume that there are no blazars below $z = 0.01$ [4].

The cumulative intensity energy spectrum dI/dE_γ of *all* blazars (i.e. resolved and unresolved) can be computed (in units of $\text{cm}^{-2} \text{s}^{-1} \text{sr}^{-1} \text{GeV}^{-1}$) as follows:

$$\frac{dI}{dE_\gamma} = \int_{0.01}^{5.0} dz \frac{dV}{dz} \int_1^{3.5} d\Gamma \int_{L_{\min}}^{L_{\max}} dL_\gamma \Phi(L_\gamma, z, \Gamma) \times F(L_\gamma, z, \Gamma) \frac{dN_\gamma(\Gamma, z, E_\gamma)}{dE_\gamma}. \quad (10)$$

Similarly to Eq. (9), $F(L_\gamma, z, \Gamma)$ is the flux (between 0.1 and 100 GeV) produced by a source with luminosity L_γ , spectral index Γ and at a redshift z , and dN_γ/dE_γ is the energy spectrum from Eq. (8), properly normalized so that $F dN_\gamma/dE$ provides the differential flux of the source. The upper bound in the integration in L_γ is fixed at $10^{52} \text{erg s}^{-1}$ and the lower one at $10^{43} \text{erg s}^{-1}$. Their precise value is not particularly important as the integrand in Eq. (10) drops quickly at low and high luminosities.

Finally, for the APS $C_P^{i,j}$ between energy bins i and j ($i = j$ for the auto-correlation APS and otherwise for the cross-correlation), we assume that blazars are point-like and that their APS is dominated by their so-called

1-halo term [5, 46]. This is a good assumption if the sources producing the anisotropy signal are relatively bright and not numerous, which is the case for unresolved blazars [5, 6]. In that case, the APS is Poissonian, i.e., independent of angular multipoles. It can be computed as follows (in units of $\text{cm}^{-4} \text{s}^{-2} \text{sr}^{-1}$):

$$C_P^{i,j} = \int_{0.01}^{5.0} dz \frac{dV}{dz} \int_1^{3.5} d\Gamma \int_{L_{\min}}^{L_{\max}} dL_\gamma \Phi(L_\gamma, z, \Gamma) \times F_i(L_\gamma, z, \Gamma) F_j(L_\gamma, z, \Gamma) \times [1 - \Omega(F_E(L_\gamma, z, \Gamma), \Gamma)]. \quad (11)$$

The quantity $\Omega(F, \Gamma)$ is the so-called ‘‘sky coverage’’ and it describes the probability of *Fermi* LAT to resolve a source characterized by (F, Γ) . It accounts for the fact that the telescope has a lower (i.e. better) sensitivity for harder sources. Note that the number fluxes F_i and F_j are integrated inside energy bins i and j , respectively, while the energy flux F_E in the sky coverage is integrated between 0.1 and 100 GeV. However, we ignore the exact behaviour of Ω and the estimated $C_P^{i,j}$ is very sensitive to how one models the transition between resolved and unresolved sources. Therefore, we decide to follow the procedure adopted in Ref. [16] and we compute $C_P^{i,j}$ as the difference of two terms, i.e. $C_P^{i,j} = C_{P, \text{cov}=1}^{i,j} - C_{P, \text{cat}}^{i,j}$.

Here, $C_{P, \text{cov}=1}^{i,j}$ is the APS produced by all sources up to a certain threshold F_{thr} large enough that $\Omega(F_{\text{thr}}, \Gamma) = 1$, for all values of Γ . This threshold depends on the energy bin considered and $C_{P, \text{cov}=1}^{i,j}$ is computed as in Eq. (11) but replacing the factor $(1 - \Omega)$ with $\Theta(F_{\text{thr}}^i - F^i)\Theta(F_{\text{thr}}^j - F^j)$, where $\Theta(x)$ is the Heaviside step function. The second term $C_{P, \text{cat}}^{i,j}$ is the APS of the sources resolved in the catalogue. It is computed directly from the catalogue for all sources fainter than F_{thr} and located at $|b| > 30^\circ$. The fluxes F^i and F^j employed to compute $C_{P, \text{cat}}^{i,j}$ are obtained by integrating the best-fit spectral model of each source, as provided in the catalogue. For the *Fermi* LAT Second Source Catalogue (2FGL) [47] and 3FGL catalogues, it is known that those fits are not reliable for energies larger than few tens of GeV and, therefore, we only consider the APS $C_{P, \text{cat}}^{i,j}$ for energies below 50 GeV. By explicitly subtracting the contribution of resolved blazars, our method estimates the APS of the unresolved ones without having to assume a specific shape for the sky coverage. Ref. [16] tested that this procedure does not depend on the value chosen for F_{thr} , as long as it lies in a region with coverage equal to 1.

Table I shows the values of $C_{P, \text{cat}}^{i,j}$ for all the independent combinations of the first 10 energy bins considered in Ref. [34] and in the case of the 3FGL catalogue. The last row shows the values of F_{thr} employed for the different energy bins. Table II contains the same information but for the 2FGL catalogue.

To conclude, we note that, contrary to $C_P^{i,j}$, the way we compute the source count distribution in Eq. (9) and the intensity energy spectrum in Eq. (10) is independent of the telescope sensitivity and it is not associated with

TABLE I. Value of $C_{\text{P,cat}}^{i,j}$ (in units of $\text{cm}^{-4} \text{s}^{-2} \text{sr}^{-1}$) for all the independent combinations of the first 10 energy bins considered in Ref. [34] and for the 3FGL catalogue. The last row contains the values of F_{thr} (in units of $10^{-10} \text{cm}^{-2} \text{s}^{-1}$) employed to compute $C_{\text{P,cov}=1}^{i,j}$.

Energy [GeV]	0.50-0.72	0.72-1.04	1.04-1.38	1.38-1.99	1.99-3.15	3.15-5.00	5.00-7.23	7.23-10.45	10.45-21.83	21.83-50.00
0.50-0.72	1.15×10^{-17}									
0.72-1.04	6.51×10^{-18}	4.23×10^{-18}								
1.04-1.38	1.42×10^{-18}	8.84×10^{-19}	4.41×10^{-19}							
1.38-1.99	1.75×10^{-18}	1.10×10^{-18}	3.94×10^{-19}	4.85×10^{-19}						
1.99-3.15	1.59×10^{-18}	1.02×10^{-18}	3.00×10^{-19}	3.62×10^{-19}	3.91×10^{-19}					
3.15-5.00	1.08×10^{-18}	6.89×10^{-19}	1.79×10^{-19}	2.11×10^{-19}	2.23×10^{-19}	2.05×10^{-19}				
5.00-7.23	4.48×10^{-19}	2.88×10^{-19}	8.22×10^{-20}	9.67×10^{-20}	1.02×10^{-19}	8.06×10^{-20}	3.96×10^{-20}			
7.23-10.45	2.78×10^{-19}	1.78×10^{-19}	5.25×10^{-20}	6.09×10^{-20}	6.38×10^{-20}	5.12×10^{-20}	2.45×10^{-20}	1.76×10^{-20}		
10.45-21.83	2.54×10^{-19}	1.63×10^{-19}	4.92×10^{-20}	5.71×10^{-20}	5.83×10^{-20}	4.52×10^{-20}	2.19×10^{-20}	1.51×10^{-20}	1.70×10^{-20}	
21.83-50.00	1.06×10^{-19}	6.75×10^{-20}	1.98×10^{-20}	2.26×10^{-20}	2.33×10^{-20}	1.87×10^{-20}	8.59×10^{-21}	5.96×10^{-21}	6.32×10^{-21}	3.51×10^{-21}
F_{thr}	5.0	3.0	1.0	1.0	0.9	0.7	0.3	0.2	0.2	0.1

TABLE II. The same as Table I but for the 2FGL catalogue.

Energy [GeV]	0.50-0.72	0.72-1.04	1.04-1.38	1.38-1.99	1.99-3.15	3.15-5.00	5.00-7.23	7.23-10.45	10.45-21.83	21.83-50.00
0.50-0.72	2.42×10^{-17}									
0.72-1.04	1.08×10^{-17}	6.86×10^{-18}								
1.04-1.38	8.56×10^{-19}	5.64×10^{-19}	2.96×10^{-19}							
1.38-1.99	1.38×10^{-18}	8.72×10^{-19}	2.75×10^{-19}	4.06×10^{-19}						
1.99-3.15	1.21×10^{-18}	7.53×10^{-19}	1.99×10^{-19}	2.81×10^{-19}	2.63×10^{-19}					
3.15-5.00	1.13×10^{-18}	6.79×10^{-19}	1.21×10^{-19}	1.69×10^{-19}	1.51×10^{-19}	1.47×10^{-19}				
5.00-7.23	3.94×10^{-19}	2.32×10^{-19}	4.55×10^{-20}	6.47×10^{-20}	5.93×10^{-20}	4.72×10^{-20}	2.36×10^{-20}			
7.23-10.45	5.10×10^{-19}	2.92×10^{-19}	4.40×10^{-20}	5.73×10^{-20}	4.91×10^{-20}	4.60×10^{-20}	1.53×10^{-20}	2.63×10^{-20}		
10.45-21.83	4.42×10^{-19}	2.50×10^{-19}	3.58×10^{-20}	4.81×10^{-20}	4.13×10^{-20}	4.03×10^{-20}	1.47×10^{-20}	2.23×10^{-20}	2.26×10^{-20}	
21.83-50.00	1.68×10^{-19}	9.27×10^{-20}	1.12×10^{-20}	1.60×10^{-20}	1.35×10^{-20}	1.41×10^{-20}	4.87×10^{-21}	6.82×10^{-21}	7.19×10^{-21}	3.39×10^{-21}
F_{thr}	10.0	5.0	1.3	1.3	1.0	0.7	0.3	0.3	0.3	0.13

a specific analysis or source catalogue.

III. DATA AND FITTING TECHNIQUE

The auto- and cross-correlation APS are taken from Ref. [34]. The APS is computed from flux sky maps obtained after subtracting a model for the Galactic foreground, i.e., the emission induced by the interaction of cosmic rays with the interstellar medium and radiation fields. Also, the regions of the sky where resolved sources and the Galactic foreground are largely dominated are masked. Two masks are considered separately in Ref. [34]: they both mask the Galactic plane (i.e., the region with $|b| < 30^\circ$) and few extended sources. Then, the so-called “3FGL mask” excludes the region around each of the sources in the 3FGL catalogue, while the “2FGL mask” cuts all objects in the 2FGL catalogue. Inside the multipole range considered in Ref. [34] (i.e., between $\ell = 49$ and 706), both the auto- and cross-correlation APS are found compatible with being Poissonian. We only consider the best-fit APS $C_{\text{P}}^{i,j}$ for the first 10 energy bins, i.e. below 50 GeV. The 55 independent $C_{\text{P}}^{i,j}$ are taken from Tables I and II of Ref. [34].

The data on the source count distribution, in the case of the *Fermi* LAT First Source catalog (1FGL), are taken from Fig. 14 of Ref. [35] (data set labelled “all blazars”) and they refer to emitters associated with blazars and detected in the energy range between 100 MeV and 100 GeV. Note that these data have already been corrected for the sky coverage, so that we can directly compare them with the model prediction computed in Eq. (9). For the 2FGL and 3FGL catalogue, the dN/dF

is computed directly from the list of sources as discussed in Appendix B of Ref. [15]². We restrict ourselves to a regime in flux in which the catalogues are complete, i.e. above $1.98 \times 10^{-8} \text{cm}^{-2} \text{s}^{-1}$ for 2FGL and above $1.34 \times 10^{-8} \text{cm}^{-2} \text{s}^{-1}$ for 3FGL.³

Finally, we will also consider the intensity energy spectrum of the so-called extragalactic gamma-ray background (EGB), i.e. the residual emission observed by *Fermi* LAT after subtracting a model of the Galactic foreground [3]. The EGB is interpreted as the emission of all sources (both resolved and unresolved), as opposed to the IGRB that only includes unresolved ones. The measurement in Ref. [3] is based on 50 months of data and it covers the energy range between 100 MeV and 820 GeV. We consider the entries from Table 3 of Ref. [3], in the case of its “model A” for the Galactic foreground. Note that, in the following, we will not include the data of the EGB intensity energy spectrum in our fits. However, we will compare them to our prediction for the total emission associated with blazars.

The fits are performed by scanning over the parameters defining the blazar population and computing the likelihood function. Scans are performed with PyMultiNest⁴ [48], based on MultiNest v3.10⁵ [49–51]. The tolerance is fixed at 0.5 with 5000 live points. This guarantees a good sampling of the likelihood so that

² Here, we consider sources detected with a significance larger than 6σ , at Galactic latitudes $|b| > 30^\circ$ and associated with blazars, i.e. classes **bzb**, **bzq** and **agu** for the 2FGL catalogue and classes **b11**, **fsrq** and **bcu** for the 3FGL one.

³ Both fluxes are computed above 100 MeV.

⁴ <http://johannesbuchner.github.io/PyMultiNest/index.html>

⁵ <https://ccpforge.cse.rl.ac.uk/gf/project/multinest/>

results of the scans can be interpreted both in a Bayesian and frequentist framework.

We assume that all the data are independent⁶ and they arise from a Gaussian probability distribution. Thus, the logarithm of the likelihood function $\ln \mathcal{L}(\Theta)$ is proportional to $-\sum_i [\bar{D}_i - D_i(\Theta)]^2 / 2\bar{\sigma}_i^2$, where the sum runs over all the data considered. \bar{D}_i is the measured value for data point i and $\bar{\sigma}_i$ its estimated error, while $D_i(\Theta)$ is the value of the same observable estimated for point Θ in the parameter space. Different scans will feature different parameter spaces and different data sets.

We start by considering a parameter space that is 4-dimensional, comprised of parameters A , γ_1 , L_0 , and p_2^0 defined in Eqs. (1) and (7). The choice is made in order to guarantee a significant freedom and variability for the theoretical predictions, without having to deal with too many free parameters. In particular, γ_1 controls the gamma-ray luminosity function in the low-luminosity regime, while A and L_0 its overall normalization. The parameter p_2^0 determines the evolution of blazars with redshift. All the other parameters in Eqs. (1), (2), (5)-(8) are fixed to their median values from Ref. [4] (in the case of the LDDE evolutionary scheme). In particular, $\gamma_2 = 1.83$, $\mu^* = 2.22$, $\beta = 0.10$, $\sigma = 0.28$, $z_c^* = 1.25$, $\alpha = 7.23$, $p_1^0 = 3.39$, $\tau = 3.16$, $\delta = 0.64$, $\gamma_a = 1.7$ and $\gamma_b = 2.6$. We implement log-priors on A and L_0 (between 10^{-6} and 10^2 Gpc $^{-3}$ and between 10^{45} and 10^{53} erg s $^{-1}$, respectively) and linear priors on γ_1 and p_1^0 (between 0 and 5, and between -20 and 0, respectively). Different parameter spaces and prior distributions will be defined in the following sections.

For all the parameters Θ_i we compute the marginalized probability distribution function and the Profile Likelihood (PL). The former is obtained by integrating the posterior probability distribution over all parameters except Θ_i , while the PL is computed by maximizing over them [52, 53]. We also derive two-dimensional marginalized posterior distribution functions and PL for certain combinations of parameters. In all the cases considered, the frequentist (i.e., maximization of the likelihood) and the Bayesian (i.e., marginalization of the posterior distribution) approach yield similar results. Thus, in the following sections, we show only the frequentist case.

IV. RESULTS

A. Fitting only the auto- and cross-correlation angular power spectrum (3FGL mask)

We start by performing a scan over A , γ_1 , L_0 and p_2^0 , and by computing the likelihood only in terms of the auto- and cross-correlation APS from Ref. [34] for the 3FGL mask. The solid red lines in Fig. 1 shows the derived one-dimensional PL for the four model parameters. The red circles near the bottom of the panels indicate the best-fit points and the corresponding red (pink) horizontal lines the 68% (95%) confidence-level (CL) region. On the other hand, the red regions in Fig. 2 show the two-dimensional PL for different combinations of the model parameters. The inner contours denote the 68% CL region and the outer ones the 95% CL. The black circles are the best fits. It appears that the reconstruction of the model parameters is still affected by significant degeneracies. For example, the upper middle panel of Fig. 2 shows a degeneracy between A and L_0 since, for a fixed value of γ_1 , they both control the normalization of the gamma-ray luminosity function. Also, from the upper left panel, increasing (decreasing) γ_1 corresponds to a lower (larger) A , since making dN/dF steeper (shallower) increases (decreases) the total number of low-luminosity sources so that a large (smaller) normalization is needed to reproduce the measured APS. Another way of increasing the abundance of low-flux sources is to increase p_2^0 and, thus, shifting blazars to larger redshifts. Therefore, iso-PL lines in the lower middle panel are diagonal, from the lower left corner to the upper right corner of the panel.

Fig. 3 shows the predicted auto-correlation APS (left panel) and the 3FGL dN/dF (right panel), in comparison with the data points used in the fit (gray boxes). The best-fit solution is represented by the full red circles and the solid red line, embedded in the 68% (red) and 95% CL (pink) error bar. We note that, even if we do not include the measured source count distribution in our fit, the best-fit solution describes the data reasonably well (right panel of Fig. 3). On the other hand, the best fit underpredicts the auto-correlation APS in the first energy bin, but it is compatible with the measured APS at 95% CL⁷. This discrepancy is responsible for the best-fit $\chi^2 = -2 \ln \mathcal{L}$ of 80.88, corresponding to a χ^2 per degree of freedom of 1.47 and p -value of 0.005. Note also that the best-fit solution predicts negligible anisotropies above 50 GeV. We remind that, in our likelihood, we are neglecting any measured APS above that energy. The drop of the red line above 50 GeV is compatible with the fact that, at high energies, the measured APS has a detection significance lower than 3σ [34].

⁶ As discussed in Ref. [34], the covariances between two measured $C_{\mathbf{p}}^{i,j}$ are negligible. Also, we decide to work with the differential dN/dF , instead of the cumulative one $N(> F)$, so that we can neglect the covariance between the source count distribution in different flux bins.

⁷ Similarly, the best-fit solution overestimates most of the cross-correlation data points involving the first two energy bins.

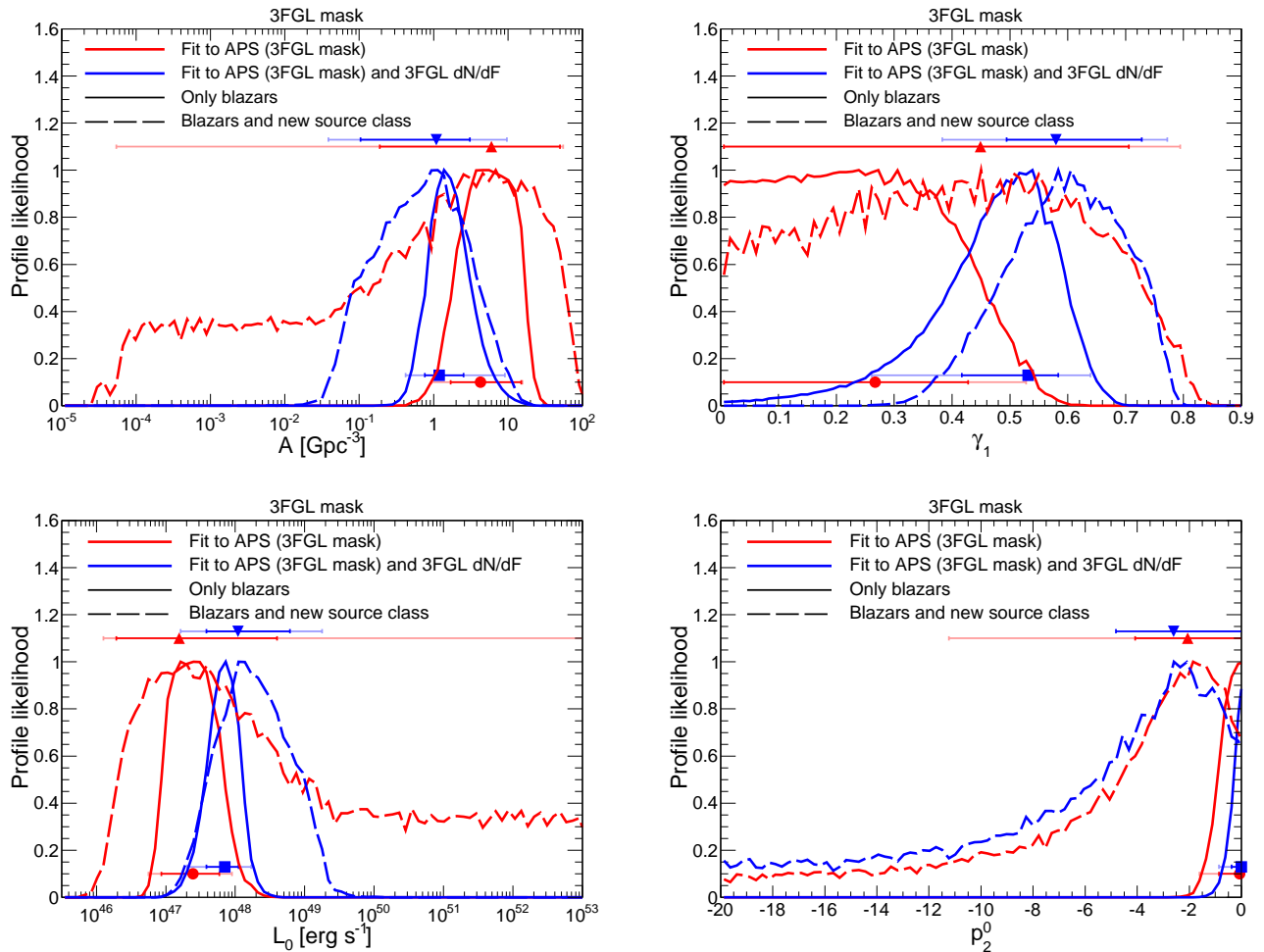


FIG. 1. One-dimensional profile-likelihood distribution for parameters A , γ_1 , L_0 and p_2^0 (see text for details). The red lines refer to the scans performed by fitting only the auto- and cross-correlation APS from Ref. [34] in the case of the 3FGL mask, while the blue lines are for the fits to the APS and the source count distribution dN/dF from the 3FGL catalogue. The solid lines refer to fits in which model predictions are computed only in terms of blazars (described by the LDDE scheme from Sec. II), while for the dashed lines we include an additional population of sources (see text). Squares, circles and triangles indicate the best-fit solutions. The sets of lines near the bottom of the panels are for the scans performed only with blazars and the ones near the top (below the legend) are for the scans including the additional source class. The horizontal lines indicate the 68% (red or dark blue) and 95% CL region (pink or light blue).

From Figs. 1 and 2 we also note that both γ_1 and p_2^0 prefer values that are at the edge of the prior range considered. This suggests that increasing the range may lead to a solution with a better χ^2 . We do not consider the possibility of negative γ_1 since there is no indication of this in the analysis of resolved blazars from Ref. [4], but we perform another scan with a prior range for p_2^0 that extends up to 20.0. Even if a positive evolution of blazars for $z > z_c$ is probably unphysical and against the findings of Ref. [4], we consider this possibility as it may increase the abundance of blazars at low energies and, thus, potentially improve the agreement with the APS below 1 GeV. However, the best-fit value for p_2^0 results to be $0.23^{+1.72}_{-0.59}$ and the best-fit APS still underproduces the low-energy APS.

B. Adding the source count distribution (3FGL mask)

A realistic model of blazars needs to reproduce the number of sources observed by *Fermi* LAT. Thus, we perform a new scan over the same four parameters as in the previous section but including the observed source count distribution dN/dF in the likelihood. We only show results for the dN/dF of the 3FGL catalogue but we performed separate scans for the 1FGL and 2FGL dN/dF . Results are qualitatively similar to what is presented in the following.

The solid blue lines in Fig. 1 show the one-dimensional PL for the four free parameters. The blue squares at the bottom of the panels mark the best-fit values and

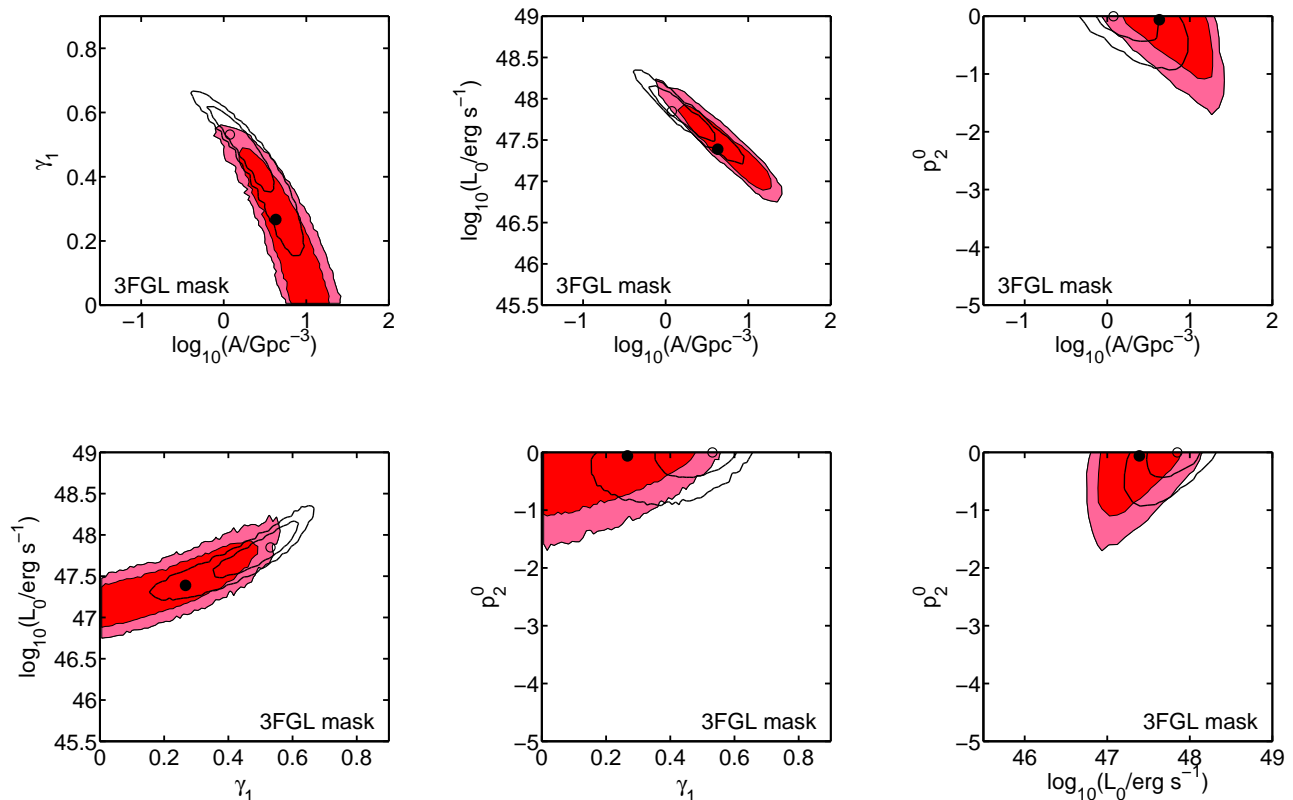


FIG. 2. Two-dimensional profile-likelihood contour plots for all the combinations of parameters A , γ_1 , L_0 and p_2^0 . Filled contours and filled black dots refer to the scans performed by fitting only the auto- and cross-correlation APS from Ref. [34] in the case of the 3FGL mask, while empty contours and empty circles are for the fits to the APS and the source count distribution dN/dF from the 3FGL catalogue. Inner contours mark the 68% CL region and outer ones the 95% CL region. The model predictions in the scans are computed only in terms of blazars.

the surrounding horizontal blue (light blue) lines the 68% (95%) CL uncertainty. The two-dimensional PL is shown in Fig. 2 by means of empty contours and the empty circle indicates the best-fit point. Overall, the precision in the estimation of the parameters has improved and the best-fit solution is not very different than what obtained when fitting only the auto- and cross-correlation APS: the preferred regions are located along the same degeneracies as before, with a slight shift towards smaller normalisations A and, therefore, a larger γ_1 and L_0 . The PL distribution for p_2^0 is still clustered towards the upper edge of its prior range, while, this time, γ_1 is different from zero at 95% CL. Solutions with a $\gamma_1 \sim 0$ would underestimate the source count distribution and, thus, are now excluded. In Fig. 4, the solid blue line and the blue squares indicate the auto-correlation APS (left panel) and the 3FGL dN/dF (right panel) corresponding to the best fit, in comparison with the data employed in the likelihood (gray boxes). The dark blue (light blue) vertical bars show the 68% and 95% CL uncertainty. Similar to the previous section, we note an underestimation of the auto-correlation APS

below 1 GeV. The best-fit solution has a χ^2 of 112.41, corresponding to a χ^2 per degree of freedom of 1.70 and a p -value of 3×10^{-4} . Allowing p_2^0 to have positive values leads to a best-fit p_2^0 that is different than zero at 95% CL (i.e. $p_2^0 = 2.48^{+0.81}_{-0.73}$). In that case, the best-fit solution has a χ^2 value of 106.10, but the reconstructed APS still underreproduces the measured one below 1 GeV. The results of these first two scans suggest that blazars alone are not able to reproduce the measured APS below the GeV scale. This agrees with the findings of Ref. [34].

We also tested this result by performing another scan in which we fit the APS with the 3FGL mask and the 3FGL dN/dF but the source count distribution is computed with all sources in the catalogue, not only blazars. In this case, the best-fit solution predicts approximately 10% more APS below 1 GeV and, thus, the best-fit χ^2 is smaller (i.e. $\chi^2 = 93.78$) than with the blazars dN/dF . This suggests that taking unassociated sources into account could improve the agreement with the measured APS. We comment more about this in Sec. V.

We note that our best-fit values from Figs. 1 and 2 are

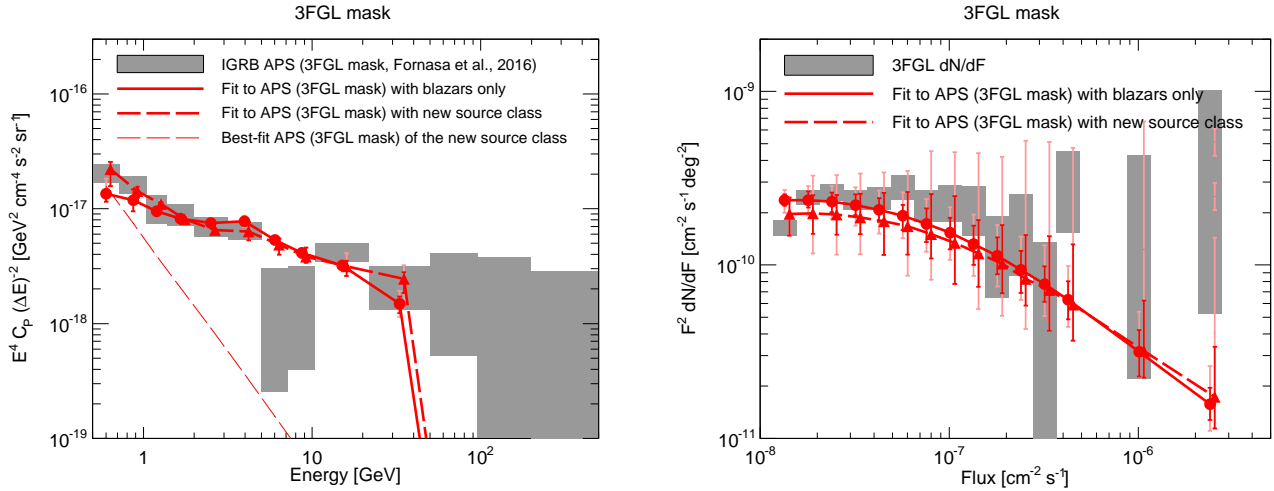


FIG. 3. The gray boxes indicate the data points used in the scans, for the auto-correlation APS with the 3FGL mask (left panel) and for the 3FGL dN/dF (right panel). The solid red lines and red circles indicate the best-fit solution for the scan performed by fitting only the auto- and cross-correlation APS from Ref. [34] (3FGL mask) with a model including only blazars. The thicker dashed red lines and the red triangles denote the best-fit solution for a scan performed fitting the same APS data but including a new source class (see text for details). The thinner red dashed line in the left panel shows the best-fit auto-correlation APS for the new class source, separately. Around each red circle/triangle, the red (pink) vertical line shows the 68% (95%) CL uncertainty. Circles and triangles are slightly shifted with respect to each other to increase readability.

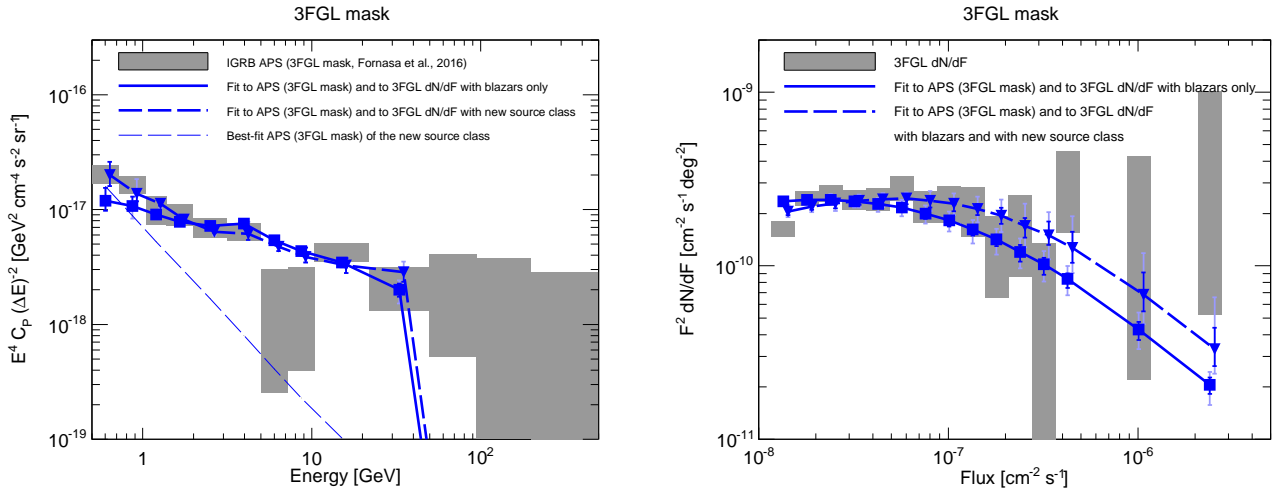


FIG. 4. The gray boxes indicate the data points used in the scans, for the auto-correlation APS with the 3FGL mask (left panel) and the 3FGL dN/dF (right panel). The solid blue lines and blue squares indicate the best-fit solution for the scan performed by fitting the auto- and cross-correlation APS from Ref. [34] (3FGL mask) and the 3FGL dN/dF , with a model including only blazars. The thicker dashed blue lines and the blue triangles denote the best-fit solution for a scan performed fitting the same APS and dN/dF data but including a new source class (see text for details). The thinner dashed blue line in the left panel shows the auto-correlation APS of the new source class, separately. Around each blue square/triangle, the dark blue (light blue) vertical line shows the 68% (95%) CL uncertainty. Squares and triangles are slightly shifted with respect to each other to increase readability.

in agreement (at the 95% CL) with the results of Ref. [4]. In that paper, the authors employ the same LDDE scheme used here to describe 403 blazars observed by *Fermi* LAT, but they used a larger parameter space and they constrained their model by fitting the blazars' flux and spectral index distributions, taking also advantage

of some redshift estimates.

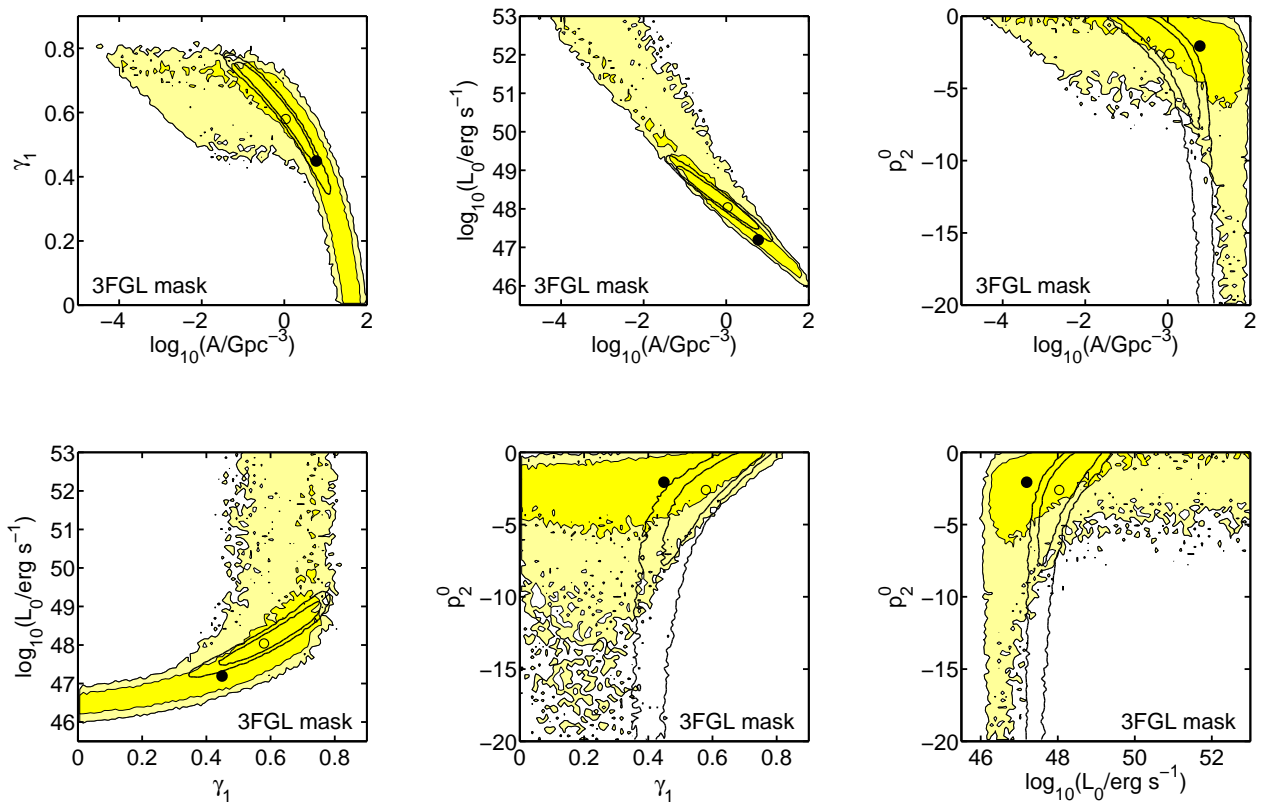


FIG. 5. Two-dimensional profile-likelihood contour plots for all the combinations of parameters A , γ_1 , L_0 and p_2^0 (see text for details). Filled contours and filled black dots refer to the scans performed by fitting only the auto- and cross-correlation APS from Ref. [34] in the case of the 3FGL mask, while empty contours and empty circles are for the fits to the APS and the source count distribution dN/dF from the 3FGL catalogue. Inner contours mark the 68% CL region and outer ones the 95% CL region. The model predictions in the scans are computed with blazars and a new class of gamma-ray emitters (see text).

C. Including a new class of sources (3FGL mask)

Motivated by the results of the previous section, we expand our theoretical model by including one additional population of sources. We adopt a phenomenological description and we assume that the new sources emit with a power-law energy spectrum ($\propto E^{-\Gamma_{\text{new}}}$) and that they are point-like and unclustered. Thus, their auto- and cross-correlation can be written as follows:

$$C_P^{i,j} = C_P^{0,0} \frac{[E_{\text{max},i}^{1-\Gamma_{\text{new}}} - E_{\text{min},i}^{1-\Gamma_{\text{new}}}] [E_{\text{max},j}^{1-\Gamma_{\text{new}}} - E_{\text{min},j}^{1-\Gamma_{\text{new}}}]}{[E_{\text{max},0}^{1-\Gamma_{\text{new}}} - E_{\text{min},0}^{1-\Gamma_{\text{new}}}]^2}, \quad (12)$$

where $C_P^{0,0}$ is the auto-correlation APS of the new population in the first energy bin, between $E_{\text{min},0}$ and $E_{\text{max},0}$, while $E_{\text{min},i}$ and $E_{\text{max},i}$ indicate the lower and upper edge of the $(i+1)$ -th energy bin.

We perform one additional scan fitting the auto- and cross-correlation APS from Ref. [34] for the 3FGL mask but adding the contribution of the new source class. Γ_{new} and $C_P^{0,0}$ are added to the list of the free parameters in the scan. We assume flat priors for Γ_{new} between

2.2 and 3.4 and log priors for $C_P^{0,0}$ between 10^{-20} and $10^{-15} \text{ cm}^{-4} \text{ s}^{-2} \text{ sr}^{-1}$.

The one-dimensional PL distributions for A , γ_1 , L_0 and p_2^0 for the new scan are plotted as red dashed lines in Fig. 1. The best fits are marked by the red triangles, within their 68% and 95% CL uncertainty denoted by the red and pink horizontal lines. The two-dimensional 68% and 95% CL regions are also shown in Fig. 5 by the dark yellow and light yellow areas, respectively. The full black circles indicate the best fit. We note that the size of the contours has increased significantly: apart from the same degeneracy present in Fig. 2 (i.e., the diagonal band between A and γ_1 , for $A > 1 \text{ Gpc}^{-3}$), a new region appears with $A < 1 \text{ Gpc}^{-3}$, $\gamma_1 > 0.5$ and $L_0 > 10^{48} \text{ erg s}^{-1}$. There is also another new region for large A and very negative p_2^0 . Models in both of these regions significantly underproduce the measured auto- and cross-APS at low energies, and therefore, they would be excluded if blazars were the only class of gamma-ray emitters in the fit.

The new source population takes care of improving the agreement with the low-energy APS. We can see

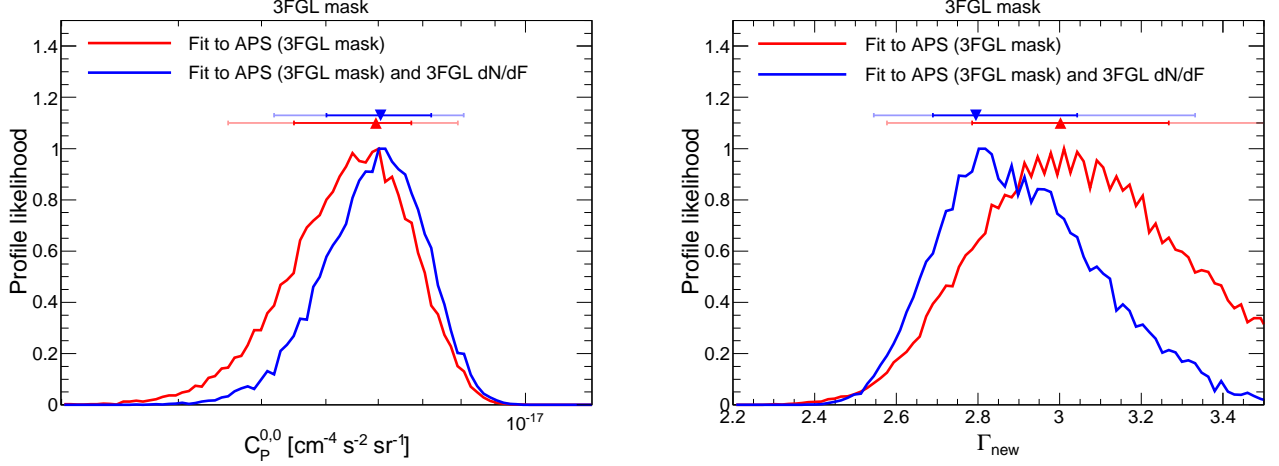


FIG. 6. As Fig. 1, but for the parameters describing the new source class.

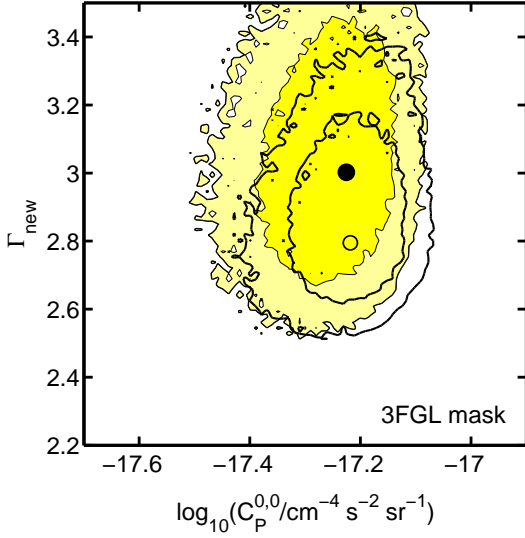


FIG. 7. Two-dimensional profile-likelihood contour plot for the parameters describing the new source class, i.e. $C_P^{0,0}$ and Γ_{new} . Filled contours and filled black dots refer to the scans performed by fitting only the auto- and cross-correlation APS from Ref. [34] in the case of the 3FGL mask, while empty contours and empty circles are for the fits to the APS and the source count distribution dN/dF from the 3FGL catalogue. Inner contours mark the 68% CL region and outer ones the 95% CL one.

this in Fig. 3, where the thick dashed red lines and the red triangles show the predicted best-fit auto-correlation APS (left panel) and 3FGL dN/dF (right panel). As before, the vertical red (pink) lines indicate the 68%

(95%) CL uncertainty. The auto-correlation APS of the new component alone is shown separately by the thinner dashed red line. The predicted dN/dF (dashed red line in the right panel) is much more uncertain than with blazars only and it systematically underproduces the 3FGL source count distribution.

Red lines in Fig. 6 show the one-dimensional PL distributions for the new parameters in the scans, i.e., $C_P^{0,0}$ (left) and Γ_{new} (right). In Fig. 7, the filled contours indicate the 68% and 95% CL regions on the $(C_P^{0,0}, \Gamma_{\text{new}})$ plane. The PL of $C_P^{0,0}$ is quite peaked and the reconstruction has a precision of 15%. The reconstruction is less precise for Γ_{new} and values between 2.79 and 3.27 are allowed at 68% CL.

The best-fit χ^2 is significantly better than without the new source class, i.e. $\chi^2 = 54.29$, corresponding to a χ^2 per degree of freedom of 1.11 and a p -value of 0.28. We can perform a likelihood-ratio test by defining $\Delta\chi^2$, i.e., the difference between the best-fit χ^2 of the simpler model (i.e. without the new source class, see Sec. IV A) and the best-fit χ^2 of the one with the new source class. Since the simpler model is located on the boundary of the more complex one, we apply Chernoff's theorem [54, 55] and obtain a p -value of 5×10^{-7} , indicating that the model with the additional source class is preferred over the interpretation in terms of only blazars at 5σ .

Alternatively, following Bayesian statistics, the comparison between models can be performed by computing the Bayes factor B , defined as the ratio of the evidences of the two scans. In our scan $\ln B$ is 12.37, a value suggesting a strong preference for the model with the new source class, according to Jeffrey's scale [56].

Finally, we perform one additional scan including the new source class but fitting both the APS (with the 3FGL mask) and the 3FGL dN/dF . The one-dimensional PL for A , γ_1 , L_0 and p_2^0 are shown as dashed blue lines (with blue triangles) in Fig. 1, while the two-dimensional PL are denoted as empty contours in Fig. 5. The most

relevant difference with respect to the fit to the APS data only (filled yellow regions in Fig. 5) is the fact that values of γ_1 smaller than 0.3 are disfavoured at 95% CL, as well as $A < 10^{-2} \text{ Gpc}^{-3}$. Solutions in those regions would underpredict or overpredict the source count distribution, respectively. Fig. 4 compares the auto-correlation APS and dN/dF of the best-fit solution (dashed thick blue lines and blue triangles) to the data (grey boxes). As for the previous case, including the new source improves the agreement with the APS data below 1 GeV. The auto-correlation APS of the new class alone is shown by the thin blue dashed line in the left panel of Fig. 4. The one-dimensional PL for $C_P^{0,0}$ and Γ_{new} are shown in Fig. 6 by blue lines and their two-dimensional PL by empty contours in Fig. 7. Results are compatible with the fit to the APS alone, confirming that the properties of the new source class do not change if we include the dN/dF data. In this case, the best-fit χ^2 is 70.19, corresponding to χ^2 per degree of freedom of 1.10 and a p -value of 0.28. The likelihood-ratio test yields a p -value of 2×10^{-10} , corresponding to more than 10σ . The presence of the new source class is strongly favoured also in a Bayesian framework as the Bayes factor $\ln B$ is 19.13.

D. Results for the 2FGL mask

We repeat the scans discussed in the previous section but we now consider the auto- and cross-APS obtained with the 2FGL mask. The solid red lines and red circles in the first four panels of Fig. 8 show the one-dimensional PL for the model parameters, in the case that the APS data are fitted only in terms of blazars (no new source class). Also, the blue regions in Fig. 9 indicate their two-dimensional PL. The contours approximately overlap with the red regions in Fig. 2, confirming that the APS data point towards the same source population, independent of the mask used. Indeed, for each of the four model parameters, the best-fit solutions obtained by using the two different masks (fitting only the APS and without additional source class) are in agreement with each other at 68% CL. The main difference between Figs. 9 and 2 is the size of the contours: for the 2FGL mask, the measurement of the auto- and cross-APS is characterized by smaller error bars than for the 3FGL mask and, therefore, a smaller portion of the parameter space can fit the data. Fig. 11 compares the APS data (left panel) and the 3FGL dN/dF (right panel) with the best-fit solution (solid red line and red circles). Differently than in Fig. 3, there is no underestimation of the APS at low energies but few discrepancies (especially for the data point around 1 GeV and around 6 GeV) yield a best-fit χ^2 of 117.24, with a χ^2 per degree of freedom of 2.30, corresponding to a p -value of 4×10^{-7} .⁸

The situation remains qualitatively unchanged if we include the 3FGL dN/dF in the fit. The solid blue lines and blue squares in Fig. 8 show the one-dimensional PL of the free parameters, while the empty contours in Fig. 9 denote the two-dimensional PL. They follow quite closely the case with only the APS data, apart from the PL of γ_1 that extends until 0.25 at 95% CL. Thus, solid blue lines in Fig. 12 are also similar to the solid red lines in Fig. 11, with no underestimate of the auto-correlation APS below 1 GeV but a systematic underestimate of the dN/dF above $3\text{--}4 \times 10^{-8} \text{ cm}^{-2} \text{ s}^{-1}$. This indicates that the likelihood is dominated by the APS measurement. The χ^2 of the best-fit solution is 166.44, corresponding to a χ^2 per degree of freedom of 2.52 and a p -value of 10^{-10} .

As in the previous section, we extend our model by including an additional source class, parametrized, as in Eq. (12) by $C_P^{0,0}$ and Γ_{new} , for which we consider the same prior ranges as before. The one-dimensional PL of the free parameters is shown in Fig. 8 by dashed lines and triangles. Red lines are for the fit to only the auto- and cross-APS and blue lines for the fit including the 3FGL dN/dF . The two-dimensional PL is shown in Fig. 10 by the green regions (fit to APS data only) and by the empty contours (fit to the APS and 3FGL dN/dF data). The full and empty circles indicate the best-fit points, respectively. As in the previous section, the size of the contours increases with respect to Fig. 9 and they include the preferred regions in Fig. 9. They are also in qualitative agreement with Fig. 5, confirming that the data sets corresponding to the two masks point towards the same blazar population. When the dN/dF data are included (blue dashed lines in Fig. 8 and empty contours in Fig. 10) there is a shift of the preferred regions to lower values of A (and thus, larger values of γ_1). However, the two sets of contours are located along the same degeneracy. These regions correspond to solutions that are in a better agreement with the 3FGL dN/dF , as it can be seen by the blue dashed lines in Fig. 12: compared to the case with blazars only (blue solid lines in Fig. 12), the better agreement with the APS data provided by the new source class increases the weight of the dN/dF data in the likelihood. Thus, the scan is strongly driven towards configurations that also provide a good description to the source count distribution.

When fitting the APS data alone (Fig. 11), the best-fit χ^2 is 74.51 (best-fit χ^2 per degree of freedom of 1.46 and p -value of 0.02). The likelihood-ratio test yields a p -value of 2×10^{-10} , corresponding to more than 10σ evidence in favour of the new source class. The strong preference is confirmed also within a Bayesian framework, with a $\ln B$ of 20.93. When we include the 3FGL dN/dF data in the fit (Fig. 12), the best-fit χ^2 is 97.78, corresponding to a best-fit χ^2 per degree of freedom of 1.53 and to a p -value of 4×10^{-3} . The p -value of the likelihood-ratio test is 4×10^{-16} and the Bayes factor $\ln B$ is 31.20. Both approaches strongly favour the presence of the new class.

Note that the best-fit values of $C_P^{0,0}$ and Γ_{new} (last

⁸ Allowing p_2^0 to be positive would improve the quality of the fit.

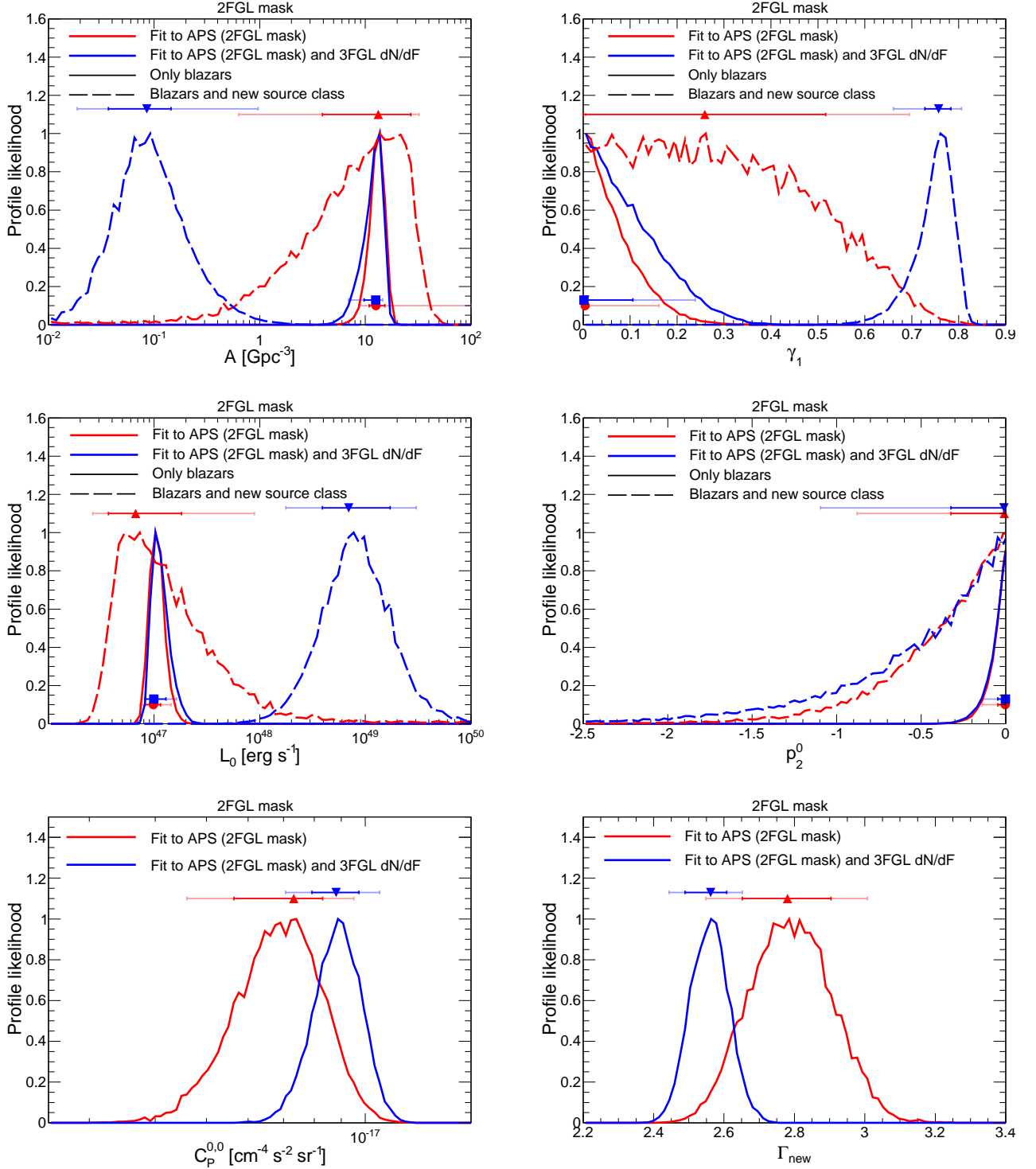


FIG. 8. One-dimensional profile-likelihood distribution for parameters A , γ_1 , L_0 , p_2^0 , $C_p^{0,0}$ and Γ_{new} (see text for details). The red lines refer to the scans performed by fitting only the auto- and cross-correlation APS from Ref. [34] in the case of the 2FGL mask, while the blue lines are for the fits to the APS and the source count distribution dN/dF from the 3FGL catalogue. The solid lines refer to fits in which model predictions are computed only in terms of blazars (described by the LDDE scheme from Sec. II), while for the dashed lines we include an additional population of sources (see text). Squares, circles and triangles indicate the best-fit solutions. The sets of lines near the bottom of the panels are for the scans performed only with blazars and the ones near the top (i.e. below the legend) are for the scans including the additional source class. The red/blue (pink/lighter blue) horizontal lines indicate the 68% (95%) CL region.

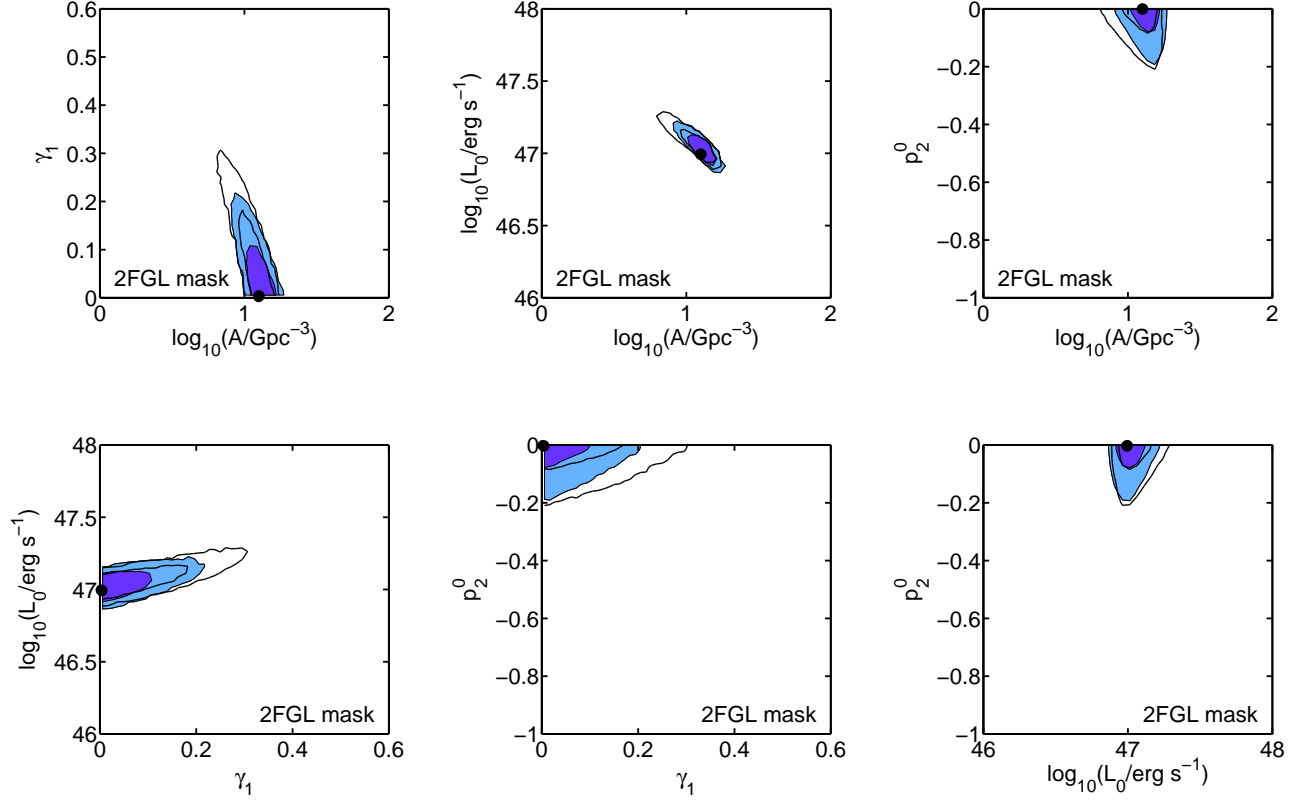


FIG. 9. Two-dimensional profile-likelihood contour plots for all the combinations of parameters A , γ_1 , L_0 and p_2^0 . Filled contours and filled black dots refer to the scans performed by fitting only the auto- and cross-correlation APS from Ref. [34] in the case of the 2FGL mask, while empty contours and empty circles are for the fits to the APS and the source count distribution dN/dF from the 3FGL catalogue. Inner contours mark the 68% CL region and outer ones the 95% CL region. The model predictions in the scans are computed including only blazars.

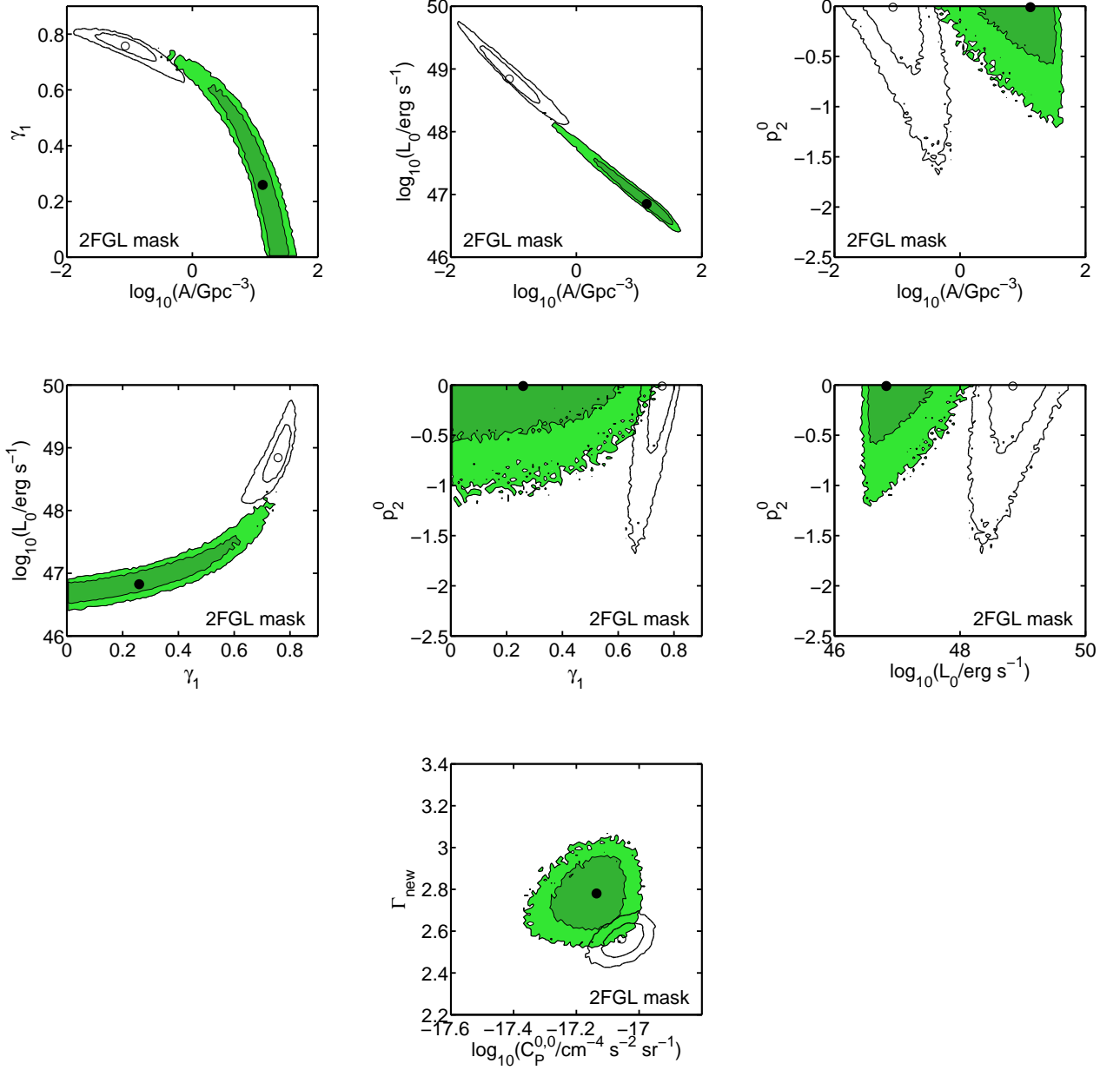


FIG. 10. Two-dimensional profile-likelihood contour plots for some combinations of parameters A , γ_1 , L_0 , p_2^0 , $C_P^{0,0}$ and Γ_{new} . Filled contours and filled black dots refer to the scans performed by fitting only the auto- and cross-correlation APS from Ref. [34] in the case of the 2FGL mask, while empty contours and empty circles are for the fits to the APS and the source count distribution dN/dF from the 3FGL catalogue. Inner contours mark the 68% CL region and outer ones the 95% CL region. The model predictions in the scans are computed with blazars and a new class of gamma-ray emitters.

panel of Fig. 10) are in agreement (at 95% CL) with the values obtained when fitting the APS with the 3FGL mask (with and without the 3FGL dN/dF data, see Fig. 7). Indeed, the auto-correlation APS associated with the new source class (thin dash line in Fig. 3, 4, 11 and 12) is very similar independently of the mask used. This might suggest that there are almost no members of the new source class with fluxes between the sensitivities of

the 3FGL and of 2FGL catalogues.

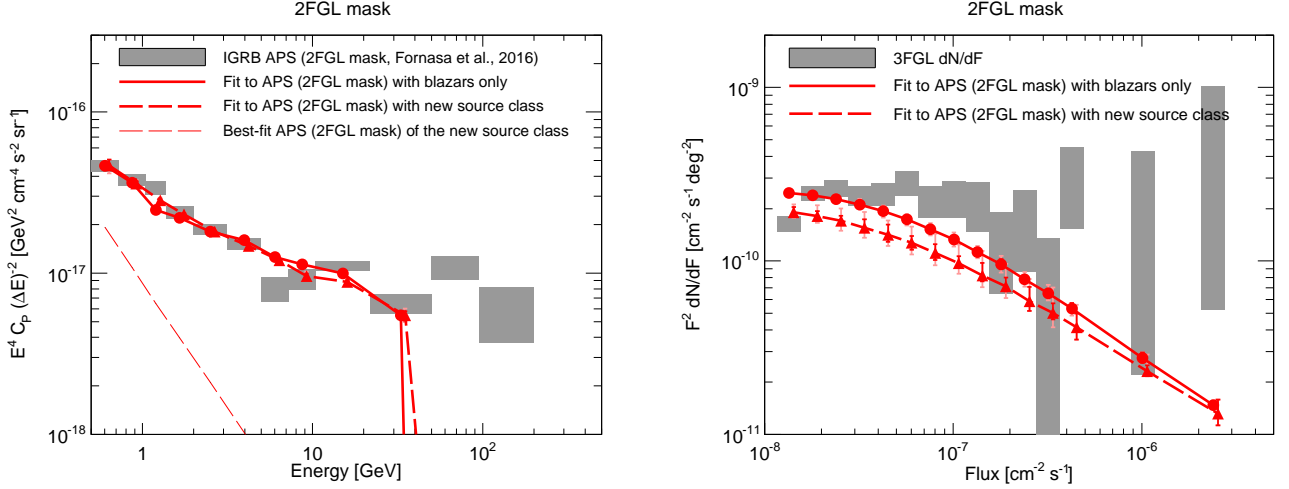


FIG. 11. The gray boxes indicate the data points used in the scans, for the auto-correlation APS with the 2FGL mask (left panel) and the 3FGL dN/dF (right panel). The solid red lines and red circles indicate the best-fit solution for the scan performed by fitting only the auto- and cross-correlation APS from Ref. [34] (2FGL mask) with a model including only blazars. The thicker dashed red lines and the red triangles denote the best-fit solutions for a scan fitting the same APS data but including a new source class (see text for details). The thinner dashed red line shows the auto-correlation APS of the new source class, separately. Around each red circle/triangle, the red (pink) vertical line shows the 68% (95%) CL uncertainty. Circles and triangles are slightly shifted with respect to each other to increase readability.

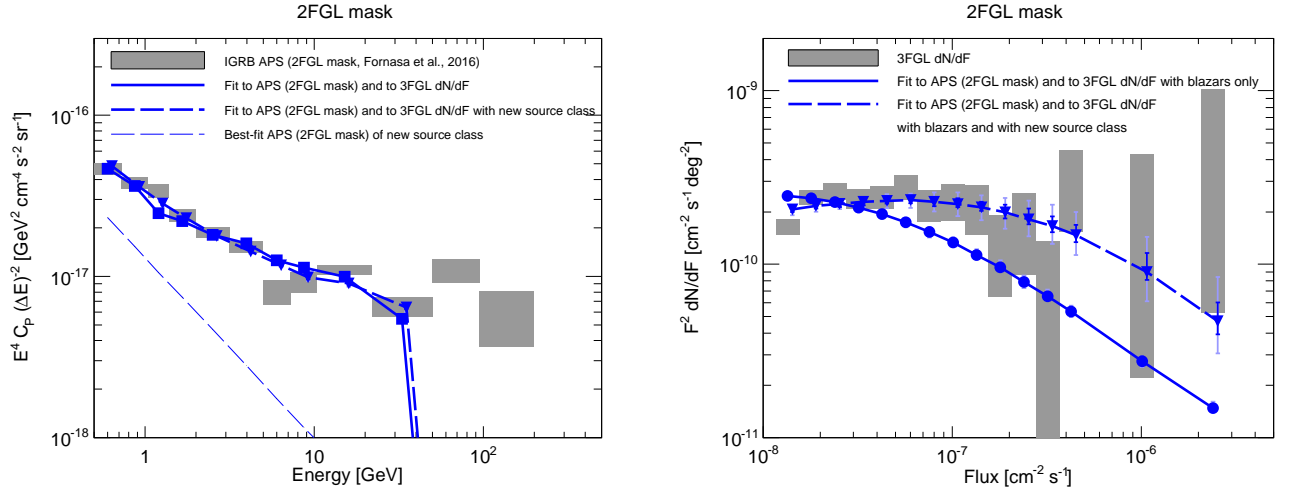


FIG. 12. The gray boxes indicate the data points used in the scans, for the auto-correlation APS with the 2FGL mask (left panel) and the 3FGL dN/dF (right panel). The solid blue lines and blue squares indicate the best-fit solution for the scan performed by fitting the auto- and cross-correlation APS from Ref. [34] (2FGL mask) and the 3FGL dN/dF , with a model including only blazars. The thicker dashed blue lines and the blue triangles denote the best-fit solution for a scan fitting the same data but including a new source class (see text for details). The thinner dashed blue line shows the auto-correlation APS of the new class, separately. Around each blue square/triangle, the blue (light blue) vertical line shows the 68% (95%) CL uncertainty. Squares and triangles are slightly shifted with respect to each other to increase readability.

V. DISCUSSION

A. Comparison with the EGB intensity energy spectrum

The gray boxes in Fig. 13 denote the EGB intensity energy spectrum from Ref. [3] (model A). We compare it

with the energy spectrum of the emission produced by all blazars (resolved and unresolved) according to the results of our scans. Top panels refer to the fits to the APS with the 3FGL mask (see Secs. IV A, IV B, and IV C), while the bottom ones to the case of the 2FGL mask (see Sec. IV D). In the left panels we show results for fits to the APS data only, while in the right ones we also

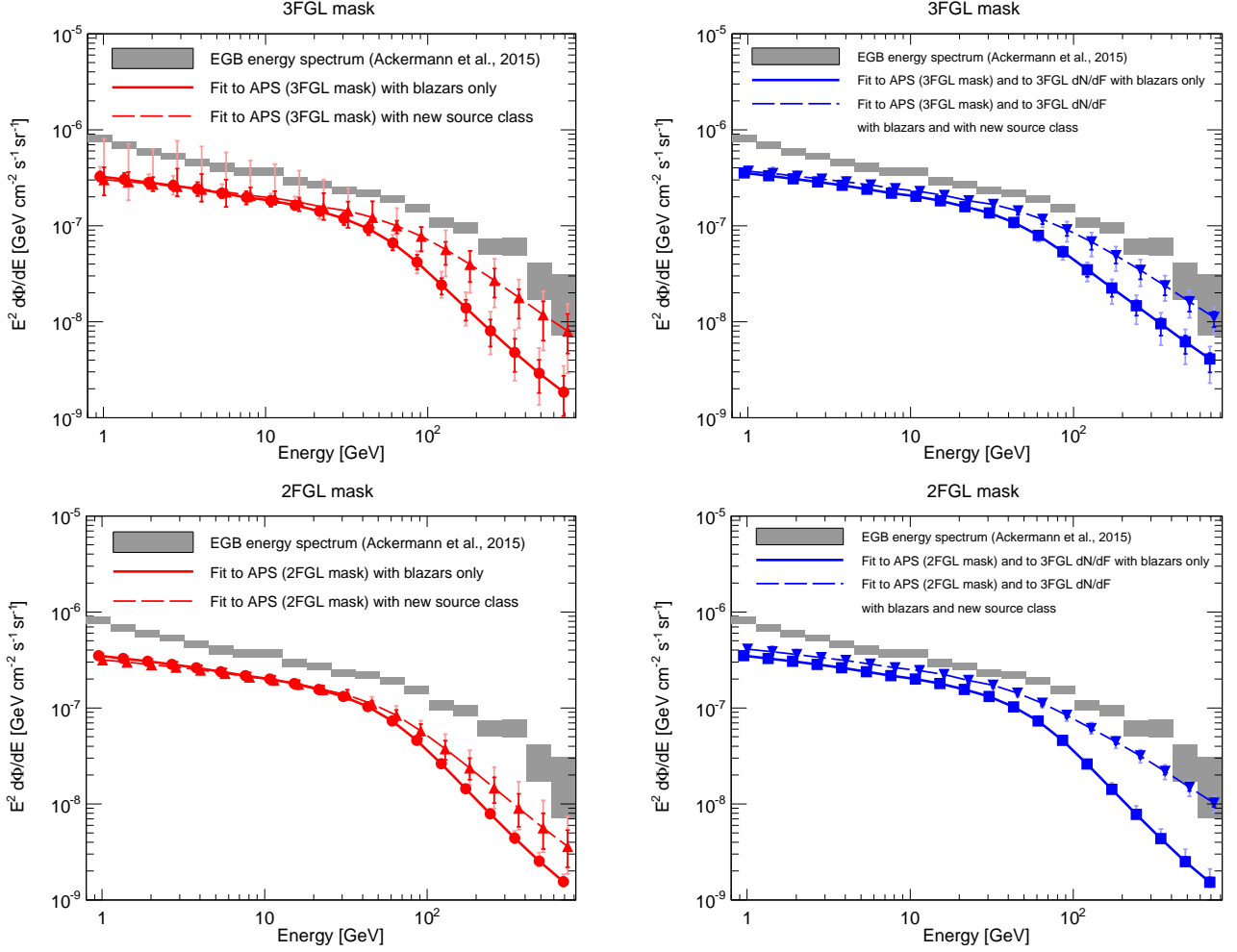


FIG. 13. The gray boxes indicate the EGB intensity energy spectrum measured in Ref. [3] (model A). (Top-left panel): The solid red line and red circles indicate the energy spectrum of the emission of all blazars (resolved and unresolved) for the best-fit solutions for the scan performed by fitting the auto- and cross-correlation APS from Ref. [34] (3FGL mask). The dashed red line and the red triangles denote the best-fit solutions for a scan performed fitting the same data but including a new source class (see text for details). (Top-right panel): The same quantities are plotted, as in the top-left panel, but for scans fitting the APS data (3FGL mask) and the 3FGL dN/dF . (Bottom panels): the same information as in the in the top panels is plotted, but for the case of the APS obtained with the 2FGL mask. In all panels, the red/blue bars around the markers indicate the 68% CL uncertainty, while the pink/light blue ones the 95% CL one. The two sets of data in each panel are slightly shifted with respect to each other to increase readability.

include the 3FGL dN/dF . Each panel contains two data sets, one for the case in which only blazars are considered in the model predictions (solid lines) and one for the fit including the new source class (dashed lines). Each data point is surrounded by its 68% CL (red or blue) and 95% CL (pink or light blue) estimated error. Note that, even when the new source class is included in the fit, Fig. 13 only shows the emission of blazars.

As pointed out in the previous sections, all the scans performed in terms of blazars only (no new sources) are in qualitative agreement (independent of which APS data are used or if the dN/dF data are included). Indeed, the four solid lines in Fig. 13 are very similar. Blazars are responsible for a fraction of the EGB above 800 MeV

that goes from 45% to 49%.

When we include the new source class (dashed lines), the emission is harder and dashed lines deviate from the solid ones around 80-100 GeV. This is probably because, since the new class account for the low-energy regime, blazars are more tuned to reproduce the behaviour at high energies. In the best-fit scenarios, blazars account for between 43% and 57% of the EGB above 800 MeV.

B. Characterization of the new source class

We start by noting that a slope Γ_{new} between approximately 2.5 and 3.2 (depending on the scan

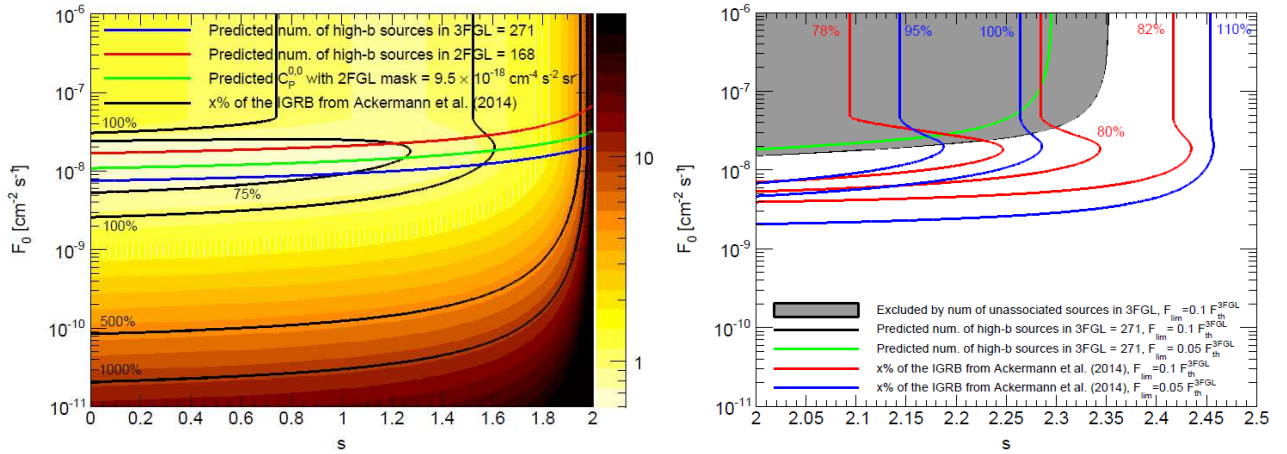


FIG. 14. (Left panel:) The colors indicate what fraction of the measured IGRB intensity can be ascribed to the new source class (above 100 MeV). The black lines mark specific levels, indicated in the labels. The blue (red) blue line shows what combination of s and F_0 correspond to a number of sources equal to 271 (168) above the 3FGL (2FGL) sensitivity and for $|b| > 30^\circ$. The green line indicates where the new source class predicts a $C_p^{0,0}$ of $9.5 \times 10^{-18} \text{ cm}^{-4} \text{ s}^{-2} \text{ sr}^{-1}$, below the 2FGL threshold. (Right panel:) The red (blue) lines indicate what combinations of s and F_0 correspond to specific fractions of the measured IGRB intensity above 100 MeV, for a $F_{\text{lim}} = 10\%$ ($F_{\text{lim}} = 5\%$) of the 3FGL sensitivity. The gray region is excluded because the new source class would overproduce the number of unassociated high-latitude emitters in the 3FGL catalogue. The black line denotes where we would have 271 sources in the 3FGL catalogue (with $|b| > 30^\circ$) and the green one where we would have 168 sources in the 2FGL one (with $|b| > 30^\circ$).

considered) is too soft to be compatible with the observed spectrum of star-forming galaxies [57, 58] (at least at ~ 1 GeV) and of misaligned active galactic nuclei [59, 60] (see, however, Ref. [61]). Also, according to Ref. [12], these two classes of gamma-ray emitters are not expected to give rise to APS as large as the one measured in Ref. [34] below 1 GeV.

Approximately one third of the sources in the 3FGL catalogue are unassociated [62]. These emitters are good candidates to play the role of the new source class uncovered in our analysis. However, these unassociated sources exhibit a harder energy spectra than what we find in our scan. The average slope for the 271 unassociated gamma-ray sources in the 3FGL catalogue detected at $|b| > 30^\circ$ is 2.26.

The inferred energy spectrum of the new source class could be in agreement with the gamma-ray emission expected from the annihilation or decay of Dark Matter in Galactic and/or extragalactic halos and subhalos. For example, a Dark Matter candidate with a mass of the order of few GeV and annihilating into b quarks would give rise to the desired energy spectrum. Many works in the literature have estimated the level of anisotropies expected for the gamma-ray emission induced by Dark Matter [5, 6, 34, 63–70]. Ref. [34] employed an hybrid method, based on the results of N -body simulations and complemented by analytical estimates. In that case, the anisotropy signal due to Dark Matter is dominated by the contribution of Galactic subhalos. However, it would be not be Poissonian, in contrast with the measured auto- and cross-APS used here.

In Ref. [34] the sub-GeV regime is where the measured

auto- and cross-APS is potentially affected by systematics related to the subtraction of the Galactic foreground, to leakage outside the mask or to specific details of data selection (see Sec. V-C of Ref. [34]). Even if it was tested that each of these effect cannot induce a deviation larger than $\sim 1\sigma$ from the final data set, maybe the simultaneous presence of difference systematics could have artificially enhanced the anisotropy expected from blazars to the level that is actually observed. This would reduce the need for the new class. The on-going measurement of gamma-ray anisotropies with Pass 8 *Fermi* LAT data will provide more information regarding this scenario.

Given the difficulty to associate the new source class with any known population of gamma-ray emitters, we attempt a phenomenological description. We assume that the new sources are well described by a broken-power-law source count distribution:

$$\frac{dN}{dF} = \begin{cases} N_0 F^{-s} & \text{for } F < F_0 \\ N_0 F^{-2.5} & \text{for } F \geq F_0 \end{cases} \quad (13)$$

The flux in Eq. (13) is defined above 100 MeV. The index above the break F_0 is fixed to the Euclidean value, i.e. 2.5, typical of sources that are homogeneously distributed in a local volume [71, 72]. This is particularly appropriate for rare emitters, as for the large-flux end of the distribution. On the contrary, the slope s below the break is left free between 0 and 2.5. We determine the normalization N_0 by requiring that the corresponding auto-APS in the first energy bins is equal to the measured

APS (with the 3FGL mask)⁹ As in Sec. II, the APS is computed as the difference of $C_{P,\text{cov}=1}$ (defined, in this case, as the integral of $F^2 dN/dF$ below the 3FGL sensitivity from the last row of Tab. I) and $C_{P,\text{cat}}$ (i.e. the APS of the sources in the 3FGL catalogue, see Tab. I). Having determined N_0 , we integrate dN/dF for each value of s and F_0 above the 3FGL sensitivity and above the 2FGL one to estimate the number of new sources expected in the 3FGL and in the 2FGL catalogue, respectively. The two sensitivities are taken from the last rows of Tab. I and II. We also compute the expected APS above the 2FGL threshold and between 0.50 and 0.72 GeV, and the integral of $F dN/dF$ above the 2FGL sensitivity. These quantities can be compared to the best-fit APS of the new source class (for the 2FGL mask, see Sec. IVD) and to the IGRB intensity from Ref. [3].

For $0 < s < 2$, all the quantities mentioned above are well defined. We summarize the scenario in the left panel of Fig. 14: colors indicate the fraction of the observed IGRB (above 100 MeV) that can be explained by the new source class. Black lines indicate the regions where the fraction is 75%, 100%, 500% and 1000%. The region below the black line labelled “100%” is not viable, disfavoring values of F_0 smaller than approximately $2 - 3 \times 10^{-9} \text{ cm}^{-2} \text{ s}^{-1}$ and value of s between 1.5 and 2.0. The blue (red) line indicates the combinations of s and F_0 that predict 271 (168) sources above the 3FGL (2FGL) sensitivity, respectively. Since these values correspond to the number of unassociated sources in the two catalogues for $|b| > 30^\circ$, the regions above the blue and red lines are also excluded. Finally, the green line indicates the combinations of s and F_0 that correspond to a $C_P^{0,0}$ of $9.5 \times 10^{-18} \text{ cm}^{-4} \text{ s}^{-2} \text{ sr}^{-1}$ when computed for the 2FGL mask. This value is the upper bound of the 95% CL interval for $C_P^{0,0}$ in the fit to the APS data with the 2FGL mask (see Fig. 10). Thus, the region above the green line is also excluded as it would be incompatible at 95% CL with the results of that fit. This leaves a narrow region around $F_0 \sim 4 \times 10^{-9} \text{ cm}^{-2} \text{ s}^{-1}$ and $s < 1.5$, in which the new source class dominates the measured IGRB intensity.

For $s \geq 2$, the computation of the IGRB intensity diverges for $F \rightarrow 0$. Thus, we introduce a cut F_{lim} below which we assume no source is present. We consider two benchmark cases for F_{lim} : 10% and 5% of the 3FGL sensitivity from Tab. I. The red (blue) lines in the right panel of Fig. 14 indicate the region where the new source class accounts for certain fractions of the observed IGRB, for the higher (lower) F_{lim} . If we consider the

higher F_{lim} , the new source class never overshoots the measured IGRB above 100 MeV, accounting for, at the most, $\sim 82\%$ of the emission. However, the gray region in the top left part of the panel is also not viable, as the new source class would predict too many sources in the 3FGL catalogue. For the lower F_{lim} , values of F_0 smaller than approximately $5 \times 10^{-9} \text{ cm}^{-2} \text{ s}^{-1}$ and of s larger than 2.26 are excluded since the new gamma-ray emitters would overproduce the measured IGRB, above 100 MeV. The region above the green line is also not viable, as it corresponds to too many unassociated sources at high latitude in the 3FGL catalogue. The only allowed area is localized around $F_0 = 10^{-8} \text{ cm}^{-2} \text{ s}^{-1}$ and for $s < 2.26$.

VI. CONCLUSIONS

In this work, we fit the recently published measurement of the IGRB anisotropy auto- and cross-APS with a physically-motivated model of blazars. Ref. [4] demonstrated that such a model provided a good description of the blazars observed by *Fermi* LAT. Here we use it to test whether blazars are able to reproduce the new APS measurement. A positive answer would confirm the result of Refs. [9, 10] (based on the original 2012 APS data [33]), according to which the IGRB APS is compatible with being due entirely to blazars. On the other hand, a negative answer would corroborate the phenomenological analysis performed in Ref. [34], establishing the need for more than one component to interpret IGRB anisotropies.

Our findings are summarized as follows:

- When fitting the new auto- and cross-APS (in the case of the 3FGL mask) in terms of blazars only, our best-fit solution is in agreement at 68% CL with the best fit obtained in Ref. [4], apart from our predicted p_2^0 , which is larger. Including the 3FGL dN/dF in the fit does not have a significant impact.
- Blazars alone (with or without including the 3FGL dN/dF in the fit) underproduce the auto- and cross-APS observed with the 3FGL mask below 1 GeV. This suggests that a different class of gamma-ray emitters is needed to reproduce the measured APS. Note that previous works analysing the IGRB anisotropies in terms of blazars (as, e.g., Refs. [9, 10]) could not be sensitive to this new source class as they were based on the 2012 APS measurement from Ref. [33], which did not extend below 1 GeV. Our result validates the findings of Ref. [34] and it suggests that sub-GeV anisotropies are due (at least in part) to gamma-ray emitters with a soft spectrum (with values of Γ_{new} ranging from 2.7 to 3.2). The properties of the new sources are consistent, whether we include the 3FGL dN/dF data in the fit or not. By a

⁹ We consider the best-fit value of $C_P^{0,0}$ from the scan performed only with the APS data (3FGL mask), see Fig. 6. Also, since we want to reproduce the auto-correlation APS in the first energy bin from Ref. [34], the integration variable is now the flux between 0.50 and 0.72 GeV. We translate the flux above 100 MeV used in Eq. 13 into the flux between 0.50 and 0.72 GeV by assuming the best-fit value for Γ_{new} from Fig. 6.

likelihood-ratio test, the new source is preferred over the blazar-only scenario by, at least, 5σ .

- If we fit the APS obtained with the 2FGL mask with blazars only, our best-fit solution does not underproduce the sub-GeV APS, as before. A new source class still improves the fit to the data and it is preferred over the blazar-only scenario by more than 10σ . However, this new source class is different than the one hinted at in Ref. [34]. In fact, in Ref. [34], the APS below 2–3 GeV (with the 2FGL mask) is almost entirely due to the population with the lower energy break (in the scenario with the sources emitting as broken power laws, i.e. the description with the lowest χ^2 per degree of freedom)¹⁰. While, in our Figs. 11 and 12 the new class is always subdominant. This indicates that the class that is responsible for the low-energy data in Ref. [34] is probably a mixture of different gamma-ray emitters, including blazars. This also attests the benefit of using a physically-motivated description of sources as we do here, instead of the phenomenological analysis performed in Ref. [34].
- When we include the new source class, the 95% CL contours point towards different regions of the parameter space, according to whether the 3FGL dN/dF data are included or not in the fit. In particular, in order to achieve a good description of the 3FGL source count distribution, γ_1 needs to be of the order of 0.75.
- The auto- and cross-correlation APS predicted by the new source class is very similar, independent of whether the scan is performed with or without the 3FGL dN/dF data, with the 2FGL or 3FGL mask. It dominates the signal below 1 GeV, in the case of the 3FGL mask and it plays a subdominant role for the 2FGL mask. This implies that no many members of the new source class are present with a flux between the 3FGL and the 2FGL sensitivity. The slope of the energy spectrum Γ_{new} goes from 2.5 to 3.2.
- The properties of the new class inferred from the fit to the APS data disagree with the characteristics of known gamma-ray emitters, e.g., star-forming galaxies or misaligned active galactic nuclei. Also, unassociated sources in the 3FGL and 2FGL catalogues have, on average, a harder energy spectrum. Dark Matter halos and subhalos can reproduce the properties of the new source class (especially for a Dark-Matter candidate with a mass of few GeV and annihilating into b quarks). However, the expected APS would probably not be Poissonian, as assumed here. Finally, the

combination of different systematic effects (i.e. contamination from Galactic foreground, leakage outside the mask and data selection) could enhance the auto- and cross-APS predicted by blazars below ~ 1 GeV, improving the agreement with the data from Ref. [34] and reducing the need for the new source class.

- We assume that the new gamma-ray emitters are characterized by a source count distribution that follows a broken power law. We leave the position of the break F_0 and the low-flux index s as free parameters. In order to reproduce the APS measurement from Ref. [34], without, at the same time, overshooting the number of unassociated sources in the 2FGL and 3FGL catalogue or the IGRB emission observed in Ref. [3], only values of F_0 around $4 \times 10^{-9} \text{ cm}^{-2} \text{ s}^{-1}$ (above 100 MeV) are allowed, for $s < 1.5$. Alternatively, assuming that there is no source belonging to the new class below a F_{lim} that is 10% of the 3FGL threshold, all considered values of F_0 and s are allowed, apart from $F_0 > 3 \times 10^{-8} \text{ cm}^{-2} \text{ s}^{-1}$ and $2 < s < 2.35$. On the other hand, if we lower F_{lim} to 5% of the 3FGL threshold, the only viable region is around F_0 of $10^{-8} \text{ cm}^{-2} \text{ s}^{-1}$ and for $2 < s < 2.27$. In all cases, the new source class would be the dominant component to the IGRB intensity.

The amount of information that we have been able to extract on the IGRB from the new APS data attests the improvement that such a measurement represents, with respect to the original 2012 one. However, it is very challenging to achieve a coherent and consistent description of the IGRB by employing only one data set. We believe that the path to conclusively dissecting the composition of the IGRB lays in the combination of multiple complementary observables. Such a longer lever arm will also clarify the nature of the new class of sources suggested by the present work.

ACKNOWLEDGMENTS

SA and MF gratefully acknowledge support from the Netherlands Organization for Scientific Research (NWO) through a Vidi grant, and MF also thanks the project MultiDark CSD2009-00064. NF, MR and HSZ acknowledge support from the research grant Theoretical Astroparticle Physics number 2012CPPYP7 under the program PRIN 2012 funded by the Ministero dell’Istruzione, dell’Università e della Ricerca (MIUR) and from the research grant TAsP (Theoretical Astroparticle Physics) funded by the Istituto Nazionale di Fisica Nucleare (INFN). HSZ gratefully acknowledges INFN for a post-doctoral fellowship in theoretical physics on “Astroparticle, Dark Matter and Neutrino Physics”, awarded under the INFN Fellowship Programme 2015.

- [1] F. Acero *et al.* (Fermi-LAT), *Astrophys. J. Suppl.* **218**, 23 (2015), arXiv:1501.02003 [astro-ph.HE].
- [2] M. Fornasa and M. A. Sanchez-Conde, *Phys. Rept.* **598**, 1 (2015), arXiv:1502.02866 [astro-ph.CO].
- [3] M. Ackermann *et al.* (Fermi-LAT), *Astrophys. J.* **799**, 86 (2015), arXiv:1410.3696 [astro-ph.HE].
- [4] M. Ajello *et al.*, *Astrophys. J.* **800**, L27 (2015), arXiv:1501.05301 [astro-ph.HE].
- [5] S. Ando, E. Komatsu, T. Narumoto, and T. Totani, *Phys. Rev. D* **75**, 063519 (2007), arXiv:astro-ph/0612467 [astro-ph].
- [6] S. Ando, E. Komatsu, T. Narumoto, and T. Totani, *Mon. Not. Roy. Astron. Soc.* **376**, 1635 (2007), arXiv:astro-ph/0610155 [astro-ph].
- [7] S. Ando and V. Pavlidou, *Mon. Not. Roy. Astron. Soc.* **400**, 2122 (2009), arXiv:0908.3890 [astro-ph.HE].
- [8] J. M. Siegal-Gaskins, R. Reesman, V. Pavlidou, S. Profumo, and T. P. Walker, *Mon. Not. Roy. Astron. Soc.* **415**, 1074 (2011), arXiv:1011.5501 [astro-ph.HE].
- [9] A. Cuoco, E. Komatsu, and J. M. Siegal-Gaskins, *Phys. Rev. D* **86**, 063004 (2012), arXiv:1202.5309 [astro-ph.CO].
- [10] J. P. Harding and K. N. Abazajian, *JCAP* **1211**, 026 (2012), arXiv:1206.4734 [astro-ph.HE].
- [11] F. Calore, M. Di Mauro, F. Donato, and F. Donato, *Astrophys. J.* **796**, 1 (2014), arXiv:1406.2706 [astro-ph.HE].
- [12] M. Di Mauro, A. Cuoco, F. Donato, and J. M. Siegal-Gaskins, *JCAP* **1411**, 021 (2014), arXiv:1407.3275 [astro-ph.HE].
- [13] D. Malyshev and D. W. Hogg, *Astrophys. J.* **738**, 181 (2011), arXiv:1104.0010 [astro-ph.CO].
- [14] M. R. Feyereisen, S. Ando, and S. K. Lee, *JCAP* **1509**, 027 (2015), arXiv:1506.05118 [astro-ph.CO].
- [15] H.-S. Zechlin, A. Cuoco, F. Donato, N. Fornengo, and A. Vittino, *Astrophys. J. Suppl.* **225**, 18 (2016), arXiv:1512.07190 [astro-ph.HE].
- [16] H.-S. Zechlin, A. Cuoco, F. Donato, N. Fornengo, and M. Regis, *Astrophys. J.* **826**, L31 (2016), arXiv:1605.04256 [astro-ph.HE].
- [17] M. Lisanti, S. Mishra-Sharma, L. Necib, and B. R. Safdi, (2016), arXiv:1606.04101 [astro-ph.HE].
- [18] J.-Q. Xia, A. Cuoco, E. Branchini, M. Fornasa, and M. Viel, *Mon. Not. Roy. Astron. Soc.* **416**, 2247 (2011), arXiv:1103.4861 [astro-ph.CO].
- [19] J.-Q. Xia, A. Cuoco, E. Branchini, and M. Viel, *Astrophys. J. Suppl.* **217**, 15 (2015), arXiv:1503.05918 [astro-ph.CO].
- [20] A. Cuoco, J.-Q. Xia, M. Regis, E. Branchini, N. Fornengo, and M. Viel, *Astrophys. J. Suppl.* **221**, 29 (2015), arXiv:1506.01030 [astro-ph.HE].
- [21] M. Regis, J.-Q. Xia, A. Cuoco, E. Branchini, N. Fornengo, and M. Viel, *Phys. Rev. Lett.* **114**, 241301 (2015), arXiv:1503.05922 [astro-ph.CO].
- [22] S. Ando, A. Benoit-Lvy, and E. Komatsu, *Phys. Rev. D* **90**, 023514 (2014), arXiv:1312.4403 [astro-ph.CO].
- [23] S. Ando, *JCAP* **1410**, 061 (2014), arXiv:1407.8502 [astro-ph.CO].
- [24] M. Shirasaki, S. Horiuchi, and N. Yoshida, *Phys. Rev. D* **92**, 123540 (2015), arXiv:1511.07092 [astro-ph.CO].
- [25] S. Ando and K. Ishiwata, *JCAP* **1606**, 045 (2016), arXiv:1604.02263 [hep-ph].
- [26] E. Branchini, S. Camera, A. Cuoco, N. Fornengo, M. Regis, M. Viel, and J.-Q. Xia, (2016), arXiv:1612.05788 [astro-ph.CO].
- [27] S. Camera, M. Fornasa, N. Fornengo, and M. Regis, *Astrophys. J.* **771**, L5 (2013), arXiv:1212.5018 [astro-ph.CO].
- [28] S. Camera, M. Fornasa, N. Fornengo, and M. Regis, *JCAP* **1506**, 029 (2015), arXiv:1411.4651 [astro-ph.CO].
- [29] M. Shirasaki, S. Horiuchi, and N. Yoshida, *Phys. Rev. D* **90**, 063502 (2014), arXiv:1404.5503 [astro-ph.CO].
- [30] M. Shirasaki, O. Macias, S. Horiuchi, S. Shirai, and N. Yoshida, (2016), arXiv:1607.02187 [astro-ph.CO].
- [31] T. Trster *et al.*, (2016), arXiv:1611.03554 [astro-ph.CO].
- [32] N. Fornengo, L. Perotto, M. Regis, and S. Camera, *Astrophys. J.* **802**, L1 (2015), arXiv:1410.4997 [astro-ph.CO].
- [33] M. Ackermann *et al.* (Fermi-LAT), *Phys. Rev. D* **85**, 083007 (2012), arXiv:1202.2856 [astro-ph.HE].
- [34] M. Fornasa *et al.*, (2016), arXiv:1608.07289 [astro-ph.HE].
- [35] A. A. Abdo *et al.* (Fermi-LAT), *Astrophys. J.* **720**, 435 (2010), arXiv:1003.0895 [astro-ph.CO].
- [36] M. Ajello *et al.*, *Astrophys. J.* **751**, 108 (2012), arXiv:1110.3787 [astro-ph.CO].
- [37] M. Ajello *et al.*, *Astrophys. J.* **780**, 73 (2014), arXiv:1310.0006 [astro-ph.CO].
- [38] Y. Inoue and T. Totani, *Astrophys. J.* **702**, 523 (2009), [Erratum: *Astrophys. J.* 728,73(2011)], arXiv:0810.3580 [astro-ph].
- [39] K. N. Abazajian, S. Blanchet, and J. P. Harding, *Phys. Rev. D* **84**, 103007 (2011), arXiv:1012.1247 [astro-ph.CO].
- [40] P. A. R. Ade *et al.* (Planck), *Astron. Astrophys.* **571**, A16 (2014), arXiv:1303.5076 [astro-ph.CO].
- [41] M. Ackermann *et al.* (Fermi-LAT), *Astrophys. J.* **743**, 171 (2011).
- [42] G. Ghisellini, L. Maraschi, and F. Tavecchio, *Mon. Not. Roy. Astron. Soc.* **396**, 105 (2009), arXiv:0903.2043 [astro-ph.CO].
- [43] E. T. Meyer, G. Fossati, M. Georganopoulos, and M. L. Lister, *Astrophys. J.* **752**, L4 (2012),

¹⁰ Private communication.

- arXiv:1203.4991 [astro-ph.HE].
- [44] A. A. Abdo (Fermi-LAT), *Astrophys. J.* **715**, 429 (2010), arXiv:1002.0150 [astro-ph.HE].
- [45] A. Dominguez *et al.*, *Mon. Not. Roy. Astron. Soc.* **410**, 2556 (2011), arXiv:1007.1459 [astro-ph.CO].
- [46] A. Cooray and R. K. Sheth, *Phys. Rept.* **372**, 1 (2002), arXiv:astro-ph/0206508 [astro-ph].
- [47] P. L. Nolan and others [The Fermi-LAT Collaboration] (Fermi-LAT), *Astrophys. J. Suppl.* **199**, 31 (2012), arXiv:1108.1435 [astro-ph.HE].
- [48] J. Buchner, A. Georgakakis, K. Nandra, L. Hsu, C. Rangel, M. Brightman, A. Merloni, M. Salvato, J. Donley, and D. Kocevski, *Astron. Astrophys.* **564**, A125 (2014), arXiv:1402.0004 [astro-ph.HE].
- [49] F. Feroz and M. P. Hobson, *Mon. Not. Roy. Astron. Soc.* **384**, 449 (2008), arXiv:0704.3704 [astro-ph].
- [50] F. Feroz, M. P. Hobson, and M. Bridges, *Mon. Not. Roy. Astron. Soc.* **398**, 1601 (2009), arXiv:0809.3437 [astro-ph].
- [51] F. Feroz, M. P. Hobson, E. Cameron, and A. N. Pettitt, (2013), arXiv:1306.2144 [astro-ph.IM].
- [52] R. Trotta, F. Feroz, M. P. Hobson, L. Roszkowski, and R. Ruiz de Austri, *JHEP* **12**, 024 (2008), arXiv:0809.3792 [hep-ph].
- [53] F. Feroz, K. Cranmer, M. Hobson, R. Ruiz de Austri, and R. Trotta, *JHEP* **06**, 042 (2011), arXiv:1101.3296 [hep-ph].
- [54] H. Chernoff and L. E. L., *Annals Math. Statist.* **25**, 579 (1954).
- [55] A. Shapiro, *International Statistical Review* **56**, 49 (1988).
- [56] R. Trotta, *Contemp. Phys.* **49**, 71 (2008), arXiv:0803.4089 [astro-ph].
- [57] M. Ackermann *et al.* (Fermi-LAT), *Astrophys. J.* **755**, 164 (2012), arXiv:1206.1346 [astro-ph.HE].
- [58] T. Linden, (2016), arXiv:1612.03175 [astro-ph.HE].
- [59] M. Di Mauro, F. Calore, F. Donato, M. Ajello, and L. Latronico, *Astrophys. J.* **780**, 161 (2014), arXiv:1304.0908 [astro-ph.HE].
- [60] D. Hooper, T. Linden, and A. Lopez, *JCAP* **1608**, 019 (2016), arXiv:1604.08505 [astro-ph.HE].
- [61] A. M. Brown, C. Boehm, J. Graham, T. Lacroix, P. M. Chadwick, and J. Silk, (2016), arXiv:1603.05469 [astro-ph.HE].
- [62] M. Ackermann *et al.* (Fermi-LAT), *Astrophys. J.* **810**, 14 (2015), arXiv:1501.06054 [astro-ph.HE].
- [63] S. Ando and E. Komatsu, *Phys. Rev.* **D73**, 023521 (2006), arXiv:astro-ph/0512217 [astro-ph].
- [64] A. Cuoco, J. Brandbyge, S. Hannestad, T. Haugboelle, and G. Miele, *Phys. Rev.* **D77**, 123518 (2008), arXiv:0710.4136 [astro-ph].
- [65] J. M. Siegal-Gaskins, *JCAP* **0810**, 040 (2008), arXiv:0807.1328 [astro-ph].
- [66] J. Zavala, V. Springel, and M. Boylan-Kolchin, *Mon. Not. Roy. Astron. Soc.* **405**, 593 (2010), arXiv:0908.2428 [astro-ph.CO].
- [67] A. Cuoco, A. Sellerholm, J. Conrad, and S. Hannestad, *Mon. Not. Roy. Astron. Soc.* **414**, 2040 (2011), arXiv:1005.0843 [astro-ph.HE].
- [68] M. Fornasa, J. Zavala, M. A. Sanchez-Conde, J. M. Siegal-Gaskins, T. Delahaye, F. Prada, M. Vogelsberger, F. Zandanel, and C. S. Frenk, *Mon. Not. Roy. Astron. Soc.* **429**, 1529 (2013), arXiv:1207.0502 [astro-ph.HE].
- [69] S. Ando and E. Komatsu, *Phys. Rev.* **D87**, 123539 (2013), arXiv:1301.5901 [astro-ph.CO].
- [70] J. M. Siegal-Gaskins and V. Pavlidou, *Phys. Rev. Lett.* **102**, 241301 (2009), arXiv:0901.3776 [astro-ph.HE].
- [71] J. A. Peacock, *Cosmological Physics* (Cambridge University Press, 1998).
- [72] S. Ando, M. R. Feyereisen, and M. Fornasa, (2017), arXiv:1701.02165 [astro-ph.HE].